Revisiting the Wintertime Intraseasonal SST Variability in the Tropical South Indian Ocean: Impact of the Ocean Interannual Variation*

YUANLONG LI AND WEIQING HAN

Department of Atmospheric and Oceanic Sciences, University of Colorado, Boulder, Boulder, Colorado

TOSHIAKI SHINODA

Department of Physical and Environmental Sciences, Texas A&M University, Corpus Christi, Texas

CHUNZAI WANG

NOAA/Atlantic Oceanographic and Meteorological Laboratory, Miami, Florida

M. RAVICHANDRAN

Indian National Centre for Ocean Information Services, Hyderabad, Andhra Pradesh, India

JIH-WANG WANG

Cooperative Institute for Research in Environmental Sciences, Boulder, Colorado

(Manuscript received 29 October 2013, in final form 11 March 2014)

ABSTRACT

Intraseasonal sea surface temperature (SST) variability over the Seychelles–Chagos thermocline ridge (SCTR; 12°–4°S, 55°–85°E) induced by boreal wintertime Madden–Julian oscillations (MJOs) is investigated with a series of OGCM experiments forced by the best available atmospheric data. The impact of the ocean interannual variation (OIV), for example, the thermocline depth changes in the SCTR, is assessed. The results show that surface shortwave radiation (SWR), wind speed–controlled turbulent heat fluxes, and wind stress–driven ocean processes are all important in causing the MJO-related intraseasonal SST variability. The effect of the OIV is significant in the eastern part of the SCTR (70°–85°E), where the intraseasonal SSTs are strengthened by about 20% during the 2001–11 period. In the western part (55°–70°E), such effect is relatively small and not significant. The relative importance of the three dominant forcing factors is adjusted by the OIV, with increased (decreased) contribution from wind stress (wind speed and SWR). The OIV also tends to intensify the year-to-year variability of the intraseasonal SST amplitude. In general, a stronger (weaker) SCTR favors larger (smaller) SST responses to the MJO forcing. Because of the nonlinearity of the upper-ocean thermal stratification, especially the mixed layer depth (MLD), the OIV imposes an asymmetric impact on the intraseasonal SSTs between the strong and weak SCTR conditions. In the eastern SCTR, both the heat flux forcing and entrainment are greatly amplified under the strong SCTR condition, but only slightly suppressed under the weak SCTR condition, leading to an overall strengthening effect by the OIV.

1. Introduction

The Madden–Julian oscillation (MJO) (Madden and Julian 1971) is the major mode of intraseasonal variability in the tropical troposphere and has a profound impact on the climate around the globe (Zhang 2005). MJOs are characterized by large-scale perturbations of deep convection and low-level winds at periods of 20–90 days. They

* Indian National Centre for Ocean Information Services Contribution Number 186.

Corresponding author address: Yuanlong Li, Department of Atmospheric and Oceanic Sciences, University of Colorado, Boulder, Campus Box 311, Boulder, CO 80309.
E-mail: yuanlong.li@colorado.edu

DOI: 10.1175/JPO-D-13-0238.1

propagate eastward over the warm waters of the tropical Indo-Pacific Ocean at a mean speed of 5 m s^{-1}. The MJO is considered an intrinsic mode of the tropical atmosphere at the lowest order (e.g., Knutson and Weickmann 1987; Wang and Rui 1990), but the importance of air–sea coupling for the MJO dynamics has been increasingly recognized (e.g., Flatau et al. 1997; Hendon and Glick 1997; Wang and Xie 1998; Waliser et al. 1999; Woolnough et al. 2000; Sengupta et al. 2001; Webber et al. 2010). Modeling studies showed that including air–sea coupling on the intraseasonal time scale can improve the simulation (e.g., Hendon 2000; Woolnough et al. 2001; Inness and Slingo 2003; Inness et al. 2003; Sperber et al. 2005; Zhang et al. 2006; Watterson and Syktus 2007) and forecast (Waliser 2005; Woolnough et al. 2007) of the MJO, despite that the degree of improvement ranges from minimal to substantial.

The air–sea coupling processes, however, are not yet well understood, leaving the prediction of the MJO a challenging task for the state-of-the-art climate models (Zhang et al. 2006; Lau et al. 2012; Sato et al. 2009; Xavier 2012; Hung et al. 2013). In the tropics, the ocean affects the atmosphere mainly through the variability of sea surface temperature (SST). Recent studies demonstrated that the upper-ocean dynamics and relevant SST variability in the tropical Indian Ocean act as a potential trigger for some of the MJO events (Webber et al. 2010, 2012a,b). Therefore, investigating the intraseasonal SST variability in the tropical Indian Ocean and its driving mechanism is a key step toward a better understanding of the MJO dynamics.

Over the Indian Ocean, the Seychelles–Chagos thermocline ridge (SCTR; defined between 12° and 4°S, 55° and 85°E in this study) (Hermes and Reason 2008) of the southwest Indian Ocean, also called the thermocline dome (McCreary et al. 1993) or the Seychelles dome (Yokoi et al. 2008, 2009), is a region of particular interest for at least three reasons. First, it is one of the regions with the largest strength of the MJO-forced intraseasonal SST variability, which often reaches 1°–2°C in boreal winter (''boreal'' omitted hereafter) (e.g., Harrison and Vecchi 2001; Duvel et al. 2004; Saji et al. 2006; Duvel and Vialard 2007; Lloyd and Vecchi 2010). Second, the SCTR is the initiation area for many of the strong wintertime MJO events (Wheeler and Hendon 2004; Zhang 2005; Webber et al. 2012a; Zhao et al. 2013). In winter, the SCTR is located under the intertropical convergence zone and characterized by high SST (>28°C). At such a high SST, relatively small changes in SST may induce significant perturbations in atmospheric convection (e.g., Gadgil et al. 1984). The feedbacks of MJO-forced SST anomalies onto the atmosphere are believed to be essential in organizing the large-scale convection, facilitating the eastward propagation of MJOs, and establishing their spatial–temporal characteristics (Saji et al. 2006; Bellenger et al. 2009; Izumo et al. 2010; Webber et al. 2012a). Third, SST variability in the SCTR region can have profound local and remote climate impacts (e.g., Xie et al. 2002; Annamalai et al. 2005, 2007; Izumo et al. 2008; Vialard et al. 2009).

Motivated by these significant aspects, many observational and modeling studies have been conducted to investigate the causes for intraseasonal SST variability in this region. Their results suggest the importance of three major processes: the surface shortwave radiation (SWR) changes associated with atmospheric convection (hereafter the SWR effect), turbulent heat fluxes controlled by wind speed (the wind speed effect), and wind stress–driven ocean processes (the wind stress effect) (e.g., Saji et al. 2006; Han et al. 2007; Li et al. 2008; Vinayachandran and Saji 2008; Vialard et al. 2008; Jayakumar et al. 2011; McPhaden and Foltz 2013). The relative importance of the three major effects is, however, still under debate. While some studies emphasized the importance of wind forcing and ocean dynamics (Harrison and Vecchi 2001; Saji et al. 2006; Han et al. 2007; Vinayachandran and Saji 2008), others suggested the dominant role of SWR (Duvel et al. 2004; Duvel and Vialard 2007; Vialard et al. 2008; Zhang et al. 2010; Jayakumar et al. 2011; Jayakumar and Gnanaseelan 2012). With the accumulation of in situ and satellite observations and the improvement of numerical models, intraseasonal SST variability in the SCTR region should be revisited to achieve a more in-depth understanding.

Intraseasonal variability of the ocean mixed layer is also influenced by processes at other time scales. At a higher frequency, the diurnal ocean variation induced by the diurnal cycle of solar radiation can modulate intraseasonal SST variability associated with the MJO. Modeling studies showed that including the diurnal cycle in ocean models amplifies the MJO-related intraseasonal SST variability by >20% in the tropical Indian and Pacific Oceans (e.g., Shinoda and Hendon 1998; Schiller and Godfrey 2003; Bernie et al. 2005, 2007; Li et al. 2013) through nonlinear effects (Shinoda 2005). Intraseasonal SST variability in the SCTR region shows also significant seasonality, with much larger amplitudes in winter. One reason for this seasonal dependence is that the MJO activities are higher in winter in the tropical south Indian Ocean, which leads to stronger heat flux and wind forcing. Another important reason is the thin mixed layer in winter (McCreary et al. 1993), which ensures a large SST response to the MJO forcing. This also implies the large sensitivity of intraseasonal SST variability to the ocean mean state.

At longer time scales, the interannual variations of the SCTR are prominent under the influence of El Niño–Southern Oscillation (ENSO) and Indian Ocean dipole (IOD; Saji et al. 1999) events, and the variability of thermocline depth is highly correlated with the local SST changes (e.g., Masumoto and Meyers 1998; Xie et al. 2002; Tozuka et al. 2010; Yokoi et al. 2012). Interannual variations of the ocean state, such as the mixed layer depth (MLD) and thermocline depth, are expected to affect the mixed layer thermal variability at the intraseasonal time scale. Jayakumar et al. (2011) showed that the wind stress–driven ocean interannual variation (OIV) modulates the intraseasonal SSTs by up to 30% of the amplitude. Besides the amplitude, how the relative importance of different processes is modulated by the OIV remains unclear. Vinayachandran and Saji (2008) proposed that heat fluxes dominate when the thermocline is deep and MLD is thick, whereas entrainment cooling tends to be important when the thermocline is shallow. Among the existing studies that address intraseasonal SST variability in the SCTR, in situ observations were obtained during different MJO events and modeling results covered different time periods. The OIV impact may reconcile some of their discrepancies. This points to the need for a systematical investigation of the OIV impact on intraseasonal SST variability.

In this study, we have two primary objectives. The first is to revisit the intraseasonal SST variability in the SCTR region associated with the MJO using the new version of the Hybrid Coordinate Ocean Model (HYCOM). The recently available, high-quality satellite-based atmospheric datasets are used as the forcing fields. The improvements in model physics, configuration, and forcing fields allow the model to better estimate the relevant upper-ocean processes. The second objective is to assess the OIV impact on both the amplitude and mechanism of the intraseasonal SSTs. In particular, the paper focuses on exploring how the interannually varying ocean mean state modulates the relative importance of the SWR, wind speed, and wind stress effects in causing intraseasonal SST variability. We hope that the devoted effort can improve our understanding of the mechanism controlling intraseasonal SST variability in an initiation area of the wintertime MJO and thereby contribute to the U.S. Dynamics of the MJO (DYNAMO) program (http://www.eol.ucar.edu/projects/dynamo/) (Zhang et al. 2013). The rest of the paper is organized as follows. Section 2 outlines the OGCM configuration and experiment design. In section 3, we describe the OIV impact on the intraseasonal SST variability in the SCTR region and explore the physical processes associated with the reported OIV impact. Section 4 provides the summary and discussion.

2. Model and experiments

a. Model configuration

The OGCM used in this study is the HYCOM, version 2.2.18, which combines isopycnal, sigma (terrain following), and z-level coordinates to optimize the representation of oceanic processes (Bleck 2002; Wallcraft et al. 2009). HYCOM is widely used by recent studies to investigate ocean processes in different regions and has proven successful in tackling problems at various spatial and temporal scales (e.g., Han et al. 2006, 2007; Kara et al. 2008; Shinoda et al. 2012; Wang et al. 2012a). In this study, we configure the model to the Indian Ocean basin (50°S–30°N, 30°–122.5°E) with a horizontal resolution of 0.25° × 0.25°. Realistic marine bathymetry from the National Geophysical Data Center (NGDC) 2′ digital data are used as the model marine topography after a 1.5° × 1.5° smoothing. The Red Sea and Persian Gulf are masked. No-slip conditions are applied along continental boundaries. At the western, eastern, and southern open-ocean boundaries 5° sponge layers are applied to relax the model temperature and salinity to the *World Ocean Atlas 2009* (*WOA09*) annual climatological values (Antonov et al. 2010; Locarnini et al. 2010). The sponge layer on the eastern boundary considers the mean temperature and salinity properties of the Indonesian Throughflow, which has been proven a feasible approach for an Indian Basin–only model experiment (e.g., Han et al. 2006, 2007; Duncan and Han 2009; Wang et al. 2012a). The model has 26 vertical layers, with layer thickness gradually enlarging from 3 m near the surface to about 500 m in the deep layer. The diffusion/mixing parameters of the model are identical to those used by Wang et al. (2012a).

The surface forcing fields of HYCOM include 2-m air temperature and humidity, surface net SWR and longwave radiation (LWR), precipitation, 10-m wind speed, and surface wind stress. The turbulent (latent plus sensible) heat fluxes are not treated as external forcing but estimated internally with the model SST, wind speed, air temperature, and specific humidity using the Coupled Ocean–Atmosphere Response Experiment, version 3.0 (COARE 3.0), algorithm (Fairall et al. 2003; Kara et al. 2005). In this study, the 2-m air temperature and humidity are adopted from the Interim European Centre for Medium-Range Weather Forecasts (ECMWF) Re-Analysis (ERA-Interim) products (Dee et al. 2011), which have a 0.75° horizontal resolution available since 1979. For the surface SWR and LWR, we use the recently available, geostationary enhanced 1° product from Clouds and the Earth's Radiant Energy System (CERES; Wielicki et al. 1996; Loeb et al. 2001) of the National Aeronautics and Space Administration (NASA) for the period of March 2000–November 2011. Li et al. (2013) compared the CERES SWR with in situ measurements by the Research Moored Array for African–Asian–Australian Monsoon Analysis and Prediction (RAMA) (McPhaden et al. 2009) and found a good agreement in both mean value and variability (correlation coefficients exceeding 0.90 at all the buoy sites). The $0.25° \times 0.25°$ cross-calibrated multiplatform (CCMP) ocean surface wind vectors available during July 1987–December 2011 (Atlas et al. 2008) are used as the wind forcing. Zonal and meridional surface wind stress, τ_x and τ_y, are calculated from the CCMP 10-m wind speed $|V|$ using the standard bulk formulas

$$\tau_x = \rho_a c_d |V| u \quad \text{and} \quad \tau_y = \rho_a c_d |V| \upsilon, \tag{1}$$

where $\rho_a = 1.175\,\mathrm{kg\,m^{-3}}$ is the air density, $c_d = 0.0015$ is the drag coefficient, and u and υ are the zonal and meridional components of 10-m winds. In our model, oceanic dynamical processes and entrainment cooling are all determined by wind stress, while wind speed affects the model SST through mainly surface turbulent heat fluxes.

The precipitation forcing is from the $0.25° \times 0.25°$ Tropical Rainfall Measuring Mission (TRMM) Multi-satellite Precipitation Analysis (TMPA) level 3B42 product (Kummerow et al. 1998) available for 1998–2011. In addition to precipitation, river discharge is also important for simulating upper-ocean salinity distribution in the Bay of Bengal (BoB) (Han and McCreary 2001), which influences the stratification and circulation of the tropical Indian Ocean. We utilize the satellite-derived monthly discharge records for the Ganga–Brahmaputra (Papa et al. 2010) and monthly discharge data from Dai et al. (2009) for the other BoB rivers, such as the Irrawaddy, as the lateral freshwater flux forcing.

b. Experiments

The model is spun up from a state of rest for 30 yr, using *WOA09* annual climatology of temperature and salinity as the initial condition. Data described above are averaged into monthly climatology to force the spinup run. Restarting from the already spun-up solution, HYCOM is integrated forward from 1 March 2000 (starting date of the CERES flux data) to 30 November 2011 (ending date of the CCMP wind data). Nine parallel experiments are performed with daily atmospheric forcing to isolate effects from different processes (see Table 1). The main run (MR) is forced with the original daily forcing. Its solution contains the complete processes and is therefore used as the reference solution and compared with observations to evaluate the model performance. To entirely exclude the MJO-related atmospheric variability, all the atmospheric forcing fields for the NoMJO experiment are low-pass filtered with a 105-day Lanczos digital filter (Duchon 1979). The difference solution, MR − NoMJO, hence measures the overall impact of MJO-related atmospheric forcing on the ocean (Table 1). There are three experiments, NoSWR, NoWIND, and NoSTRESS, designed to isolate effects of the three major forcing factors: SWR, wind speed, and wind stress. In NoSWR, we use the 105-day low-pass-filtered SWR; otherwise, the forcing fields are the same as in MR. The difference, MR − NoSWR, therefore isolates the effect of SWR forcing by the MJO. In NoWIND, both wind speed and wind stress fields are low-pass filtered, while in NoSTRESS only wind stress is low-pass filtered. The difference, NoSTRESS − NoWIND, measures the wind speed effect of the MJO, whereas MR − NoSTRESS can be used to quantify the wind stress effect.

Another group of experiments is performed to assess the impact of the OIV (Table 1). In NoOIV, we use the daily forcing fields with interannual variability removed (NoOIV forcing). With a similar method as in previous studies (e.g., Shinoda et al. 2008; Jayakumar et al. 2011), the NoOIV forcing fields are obtained by adding up the higher-frequency part (including intraseasonal variability) and the mean seasonal cycle:

$$A^* = A^H + A^{L_M}, \tag{2}$$

where A^* is the NoOIV version of a forcing variable A, A^H is the high-frequency part of A obtained through a 120-day high-pass Lanczos filter, and A^{L_M} is the time series repeating the mean seasonal cycle of A in every year. The mean seasonal cycle is derived by averaging the low-frequency part A^L time series ($A^L = A - A^H$) into one 365-day seasonal cycle. The sensitivity to the half-power period near 120 days is also examined. We find that altering the length between 105 and 135 days has little impact on the generated NoOIV variables, because the major portion of the MJO-related variance is well separated from the annual/semiannual variations in frequency space. The difference between MR and NoOIV, MR − NoOIV, can hence represent the OIV impact. NoOIV_NoSWR, NoOIV_NoWIND, and NoOIV_NoSTRESS are analogs to, respectively, NoSWR, NoWIND, and NoSTRESS, except forced with NoOIV forcing (Table 1). NoOIV − NoOIV_NoSWR, NoOIV_NoSTRESS − NoOIV_NoWIND, and NoOIV − NoOIV_NoSTRESS measure the effects of SWR, wind speed, and wind stress under no OIV impact, respectively. Comparing them with the MR − NoSWR, NoSTRESS − NoWIND, and MR − NoSTRESS solutions, we can obtain the estimates of the OIV impact on the three processes. Output from these experiments is stored in 3-day resolution for the modeling period of March 2000–November 2011. To exclude the transitioning impact from the spinup, the output in 2000 is discarded. The 11-yr record of 2001–11 is used for our analysis.

TABLE 1. HYCOM experiments and difference solutions for March 2000–November 2011. MJO signals in forcing fields are removed with a 105-day low-pass Lanczos filter (termed ''low passed'' in the table). See the text for details in generating NoOIV forcing fields.

Solution	Forcing	Description
MR	Daily forcing	Complete
NoMJO	(105 day) low-passed forcing	Remove all MJO effects
NoSWR	Low-passed SWR	Remove MJO SWR
NoWIND	Low-passed wind speed/stress	Remove MJO wind speed/stress
NoSTRESS	Low-passed wind stress	Remove MJO wind stress
NoOIV	NoOIV daily forcing	Remove OIV
NoOIV_NoSWR	NoOIV, low-passed SWR	Remove OIV and MJO SWR
NoOIV_NoWIND	NoOIV, low-passed wind	Remove OIV and MJO wind speed/stress
NoOIV_NoSTRESS	NoOIV, low-passed wind stress	Remove OIV and MJO wind stress
MR − NoMJO		Isolate total MJO forcing effect
MR − NoSWR		Isolate MJO SWR effect
NoSTRESS − NoWIND		Isolate MJO wind speed effect
MR − NoSTRESS		Isolate MJO wind stress effect
MR − NoOIV		Isolate OIV impact
NoOIV − NoOIV_NoSWR		Isolate MJO SWR effect without OIV impact
NoOIV_NoSTRESS − NoOIV_NoWIND		Isolate MJO wind speed effect without OIV impact
NoOIV − NoOIV_NoSTRESS		Isolate MJO wind stress effect without OIV impact

3. Results

a. Model/data comparison

The simulated wintertime (November–April) mean SST, sea surface salinity (SSS), MLD, and thermocline depth (represented by the depth of the 20°C isotherm Z_{20}) from the HYCOM MR are compared with satellite and in situ observational data in Fig. 1. The large-scale patterns and typical values are all consistent, albeit with some minor differences. Comparing with the SST from TRMM Microwave Imager (TMI) data (Wentz et al. 2000), the modeled SST is lower by about 0.4°C between 60° and 70°E in the SCTR region; the SSS is overestimated by 0.2–0.3 psu in the subtropical south Indian Ocean; the MLD in the Arabian Sea and BoB is overestimated by 10–20 m; and the simulated Z_{20} in the subtropical south Indian Ocean is deeper by about 20 m. These, however, have little influence on the mixed layer variability of the tropical south Indian Ocean. In the SCTR region, the mean MLD in the HYCOM MR is shallower by several meters than that from the MLD dataset based on in situ observations (Keerthi et al. 2013). Here, both the modeled and observed MLDs are calculated as the depth at which the potential density difference $\Delta\sigma$ from the surface value is equal to the density change by 0.2°C temperature decrease (de Boyer Montégut et al. 2004):

$$\Delta\sigma = \sigma(T_0 - 0.2, S_0, P_0) - \sigma(T_0, S_0, P_0), \qquad (3)$$

where T_0, S_0, and P_0 are temperature, salinity, and pressure at the sea surface, respectively. The modeled MLD is calculated for each 3-day output and averaged into the wintertime mean. As has been discussed in Li et al. (2013), possible causes of these model/data discrepancies include errors in the forcing fields, deficiency of the turbulent mixing parameterization, and also uncertainties in observational datasets. Because of the coarse vertical resolution of Argo profiles (10 m) used in the Keerthi et al. (2013) dataset, the shallow MLD feature in the western SCTR may not be fully resolved by the observational dataset. Mooring observation shows that MLD here can reach as shallow as 15 m when surface winds are weak (e.g., Vinayachandran and Saji 2008; Vialard et al. 2008). The simulated SCTR Z_{20} is systematically deeper by 10–20 m than that in the Grid Point Value of the Monthly Objective Analysis using the Argo data (MOAA GPV; Hosoda et al. 2008). The deeper thermocline in the model is, however, a common bias for existing OGCMs (e.g., Yokoi et al. 2009; Jayakumar et al. 2011; Wang et al. 2012a,b; Li et al. 2013). Albeit with these discrepancies, the comparison in Fig. 1 suggests that the model has well captured the mean state features of the upper Indian Ocean.

Before proceeding into the analysis, it is also necessary for us to check whether the OIV is properly presented in MR and successfully removed from the NoOIV experiment. Figure 2 shows the SCTR-averaged SST, MLD, and Z_{20} from the MR and NoOIV, together with those from satellite and in situ observational data. Their interannual changes are more visible in the yearly winter-mean time series. Both the 3-day and winter-mean SST from MR agree well with TMI data (Fig. 2a), with correlations of $r = 0.88$ and $r = 0.90$. Interannual changes of MLD and Z_{20} are also simulated well (Figs. 2b,c). Despite a deeper mean thermocline, the winter-mean Z_{20} correlates with that from the MOAA GPV data by $r = 0.82$,

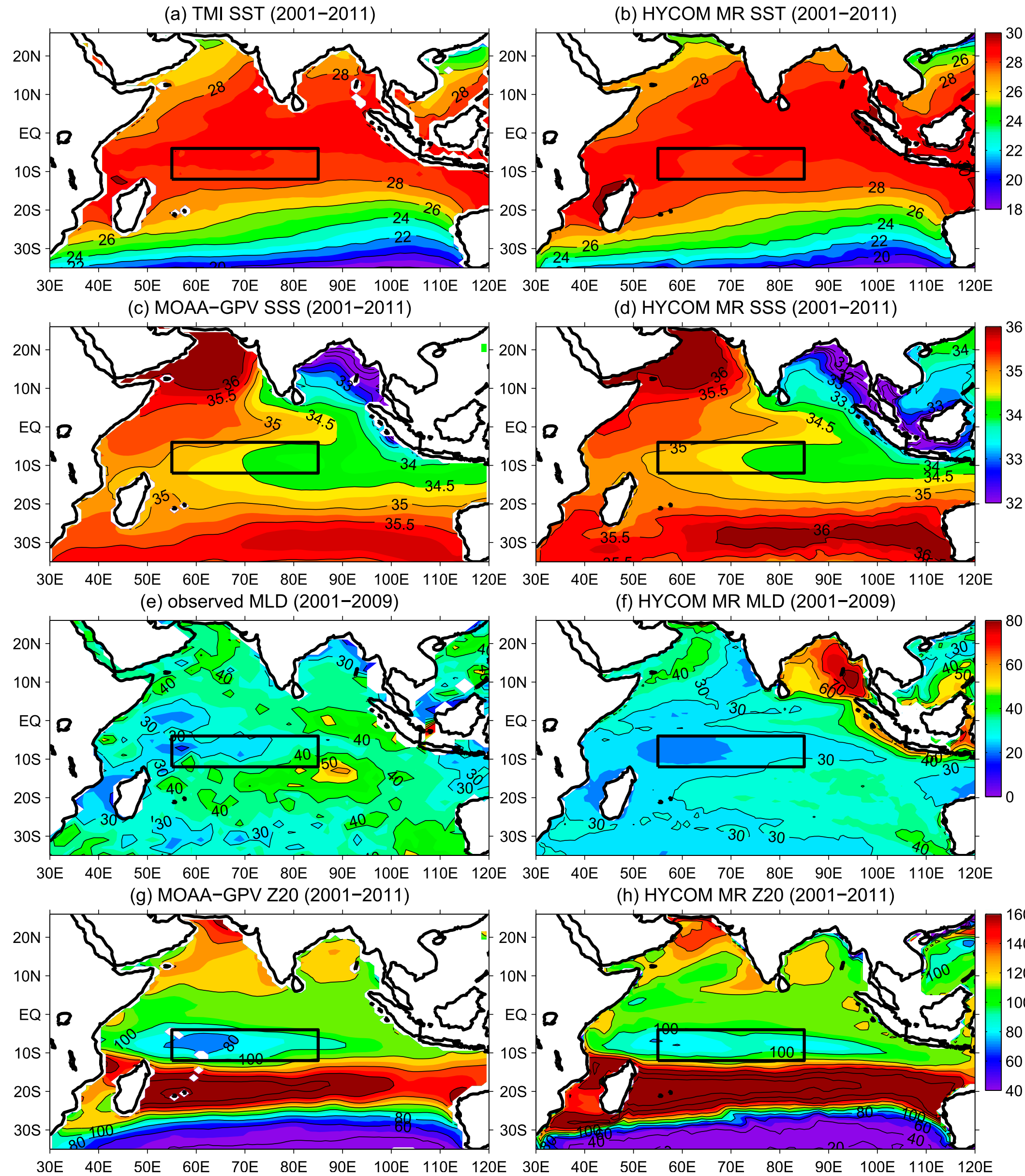

FIG. 1. Comparison of observed and modeled wintertime (November–April) mean fields. SST (°C) is given from (a) TMI satellite data and (b) HYCOM MR during 2001–11. SSS (psu) is given from (c) MOAA GPV (Hosoda et al. 2008) and (d) MR during 2001–11. MLD (m) is given from (e) Keerthi et al. (2013) and (f) MR during 2001–09. Finally, Z_{20} is given from (g) MOAA GPV and (h) MR during 2001–11. The black rectangle denotes the SCTR region (12°–4°S, 55°–85°E).

suggesting that the model can well capture the observed OIV in the SCTR. It is interesting that at an interannual time scale, a shallower (deeper) Z_{20} tends to be accompanied with cool (warm) SST and thin (thick) MLD. The linear correlation between the winter-mean modeled SST and Z_{20} is $r = 0.91$, while that between MLD and Z_{20} is $r = 0.80$. These relationships suggest the close association between subsurface ocean dynamics and mixed layer thermal variability in the SCTR region. We can also see that interannual variations in NoOIV are very weak. The small year-to-year differences in NoOIV may arise from nonlinear rectification from intraseasonal variability (e.g., Han et al. 2004; Duncan and Han 2012), but their strength is negligible when compared with the pronounced changes in MR and observation.

b. Impact in the SCTR region

The wintertime (November–April) standard deviation STD of the 20–90-day SST represents the intensity of intraseasonal SST variability. The STD pattern from MR

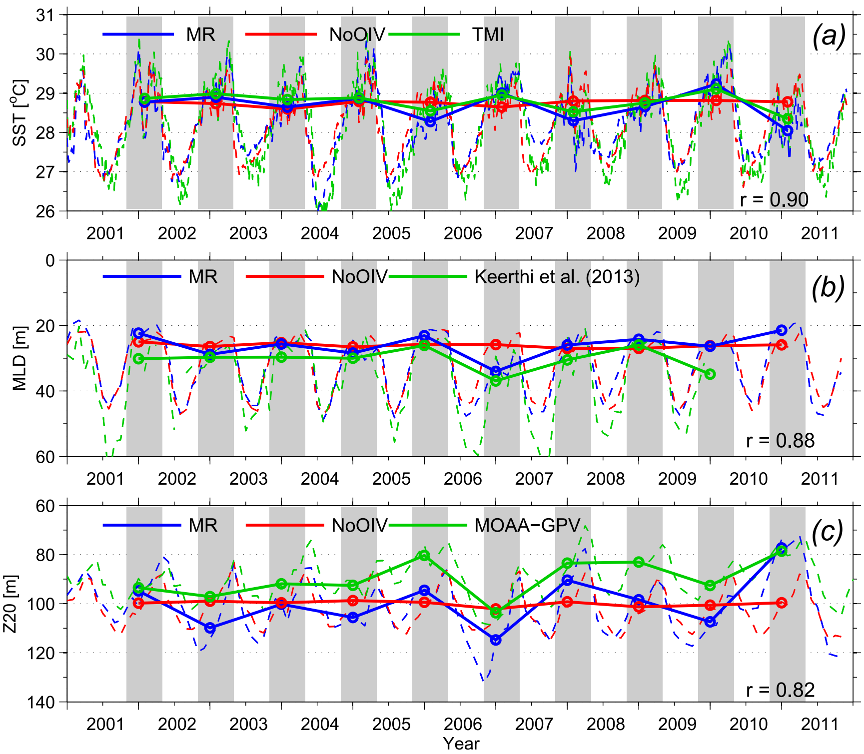

FIG. 2. (a) SST from the MR (blue), NoOIV (red), and TMI (green). Thin dashed (thick dotted) curves represent the 3-day (winter mean) SST time series. (b) Monthly (thin dashed) and winter-mean (thick dotted) MLD from MR (blue), NoOIV (red), and Keerthi et al. (2013) (green). (c) Monthly (thin dashed) and winter-mean (thick dotted) Z_{20} from MR (blue), NoOIV (red), and MOAA GPV (green). All the variables are averaged over the SCTR region (12°–4°S, 55°–85°E). The gray shadings denote the winters during 2001–11.

(Fig. 3b) agrees well with satellite observations (Fig. 3a), with high STD values centered in the tropical south Indian Ocean, the western boundary region, and the eastern BoB. In the SCTR, the region of our interest, the model has well reproduced the structure and amplitude of the intraseasonal SSTs. The STD values exceed 0.4°C in the entire SCTR box and reach 0.5°C in some areas. To isolate the SST variability associated with MJO forcing, the STD difference between MR and NoMJO, STD (MR) − STD (NoMJO), is also plotted out (Fig. 3c). Its pattern shows some evident differences from Fig. 3b. High STD values along the Somali coast are absent in Fig. 3c, confirming the dominance of ocean internal instability in producing intraseasonal SST variations there (e.g., Han et al. 2007; Vialard et al. 2012). The STD maximum in the SCTR is also much weaker than in the MR, ranging between 0.15° and 0.35°C. Hence, the MJO-forced SST changes account for about 40%–70% of the total 20–90-day SST variability. This result is not surprising. Except for extremely strong events, the amplitude of SST variability induced by MJOs is typically smaller than 0.6°C, which alone cannot yield a 0.4°–0.5°C STD value for the entire 20–90-day SST time series. Ocean internal variations, such as eddies generated by barotropic and baroclinic instability of the ocean currents, are strong in the south Indian Ocean (e.g., Jochum and Murtugudde 2005; Zhou et al. 2008). They can be responsible for a large portion (sometimes the majority) of intraseasonal SSTs at some specific grid points, but their contribution to large-scale intraseasonal SST anomalies is much smaller than the MJO forcing (Li et al. 2013). The STD difference between MR and NoOIV, STD (MR) − STD (NoOIV), represents the mean OIV impact (Fig. 3d). It exhibits an interesting spatial structure in the SCTR, with positive values >0.1°C between 70° and 85°E, which are significant at the 95% confidence level, and small negative values <0.05°C between 55° and 70°E. It means that during the winters of 2001–11, the OIV generally magnifies intraseasonal SST variability by about 20% in the eastern SCTR. In the western SCTR, the OIV slightly reduces the intraseasonal SSTs, but this change is not statistically significant. The large correction on amplitude and the interesting pattern of the OIV impact are intriguing and worthy of in-depth investigation.

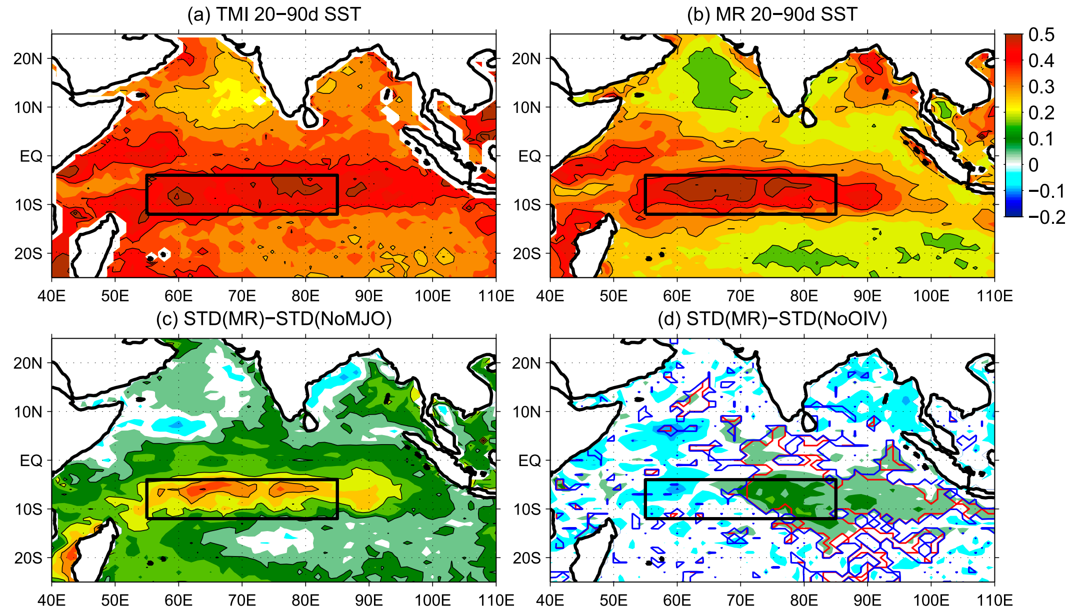

FIG. 3. STD maps of the wintertime 20–90-day SST (°C) from (a) TMI and (b) MR. (c) The STD difference of the wintertime 20–90-day SST between MR and NoMJO, that is, STD (MR) − STD (NoMJO), representing the 20–90-day SST variability induced by the total MJO forcing. (d) As in (c), but for MR and NoOIV, representing the OIV effect. The red and blue contours denote 95% and 85% confidence levels based on two-tailed F test, with the effective degrees of freedom calculated using the Bretherton et al. (1999) method. The black rectangle denotes the SCTR region.

The 20–90-day SST averaged over the SCTR region is a measure of the large-scale intraseasonal SST variability (Fig. 4). The results from MR and MR − NoMJO are very similar (Fig. 4a), with a linear correlation of r = 0.98. The wintertime (November–April) STDs are 0.27°C in MR and 0.26°C in MR − NoMJO. This agreement confirms that SCTR-averaged SST variations are predominantly caused by MJO forcing, and the ocean internal instability has little contribution to large-scale, structured, intraseasonal SST anomalies. To assess the effects of different processes, we show the 20–90-day SSTs of MR − NoSTRESS (wind stress effect), NoSTRESS − NoWIND (wind speed effect), and MR − NoSWR (SWR effect) in Fig. 4b. The three effects exhibit similar amplitudes, with STD values of 0.11°, 0.12°, and 0.10°C, respectively. Their correlation coefficients with MR are 0.75, 0.91, and 0.80, respectively. Therefore, the three processes are all important in causing intraseasonal SST variability. The overall effect of MJO-associated wind forcing (wind stress plus wind speed), which is measured by MR − NoWIND solution (not shown), causes 0.2°C SST STD, which is 74% of the MR STD.

It is noticeable that there are discernible year-to-year differences in the relative importance of the three forcing factors. For example, the wind stress effect (red curve) is relatively larger than the other two (wind speed and SWR) during the 2001/02 and 2010/11 winters. Wind speed, on the other hand, clearly dominates over the other two in 2009/10. The OIV is a possible cause for such interannual modulations (Fig. 4c). Averaged over the entire SCTR region, the intraseasonal SSTs in NoOIV are generally weaker, particularly for the large-amplitude SST anomalies associated with strong MJO events (black and cyan curves in Fig. 4c), with the SST STD 0.03°C smaller than that of the MR. The OIV effect (MR − NoOIV; pink curve) has an STD of 0.08°C, and its correlation with the MR SST is r = 0.44 (significant at the 95% confidence level), implying a nonnegligible (~20%) contribution to the total intraseasonal SST variance in the SCTR. It is interesting that the OIV impact is not always enhancing SST variability. The 20–90-day SSTs of the MR are obviously stronger than that of NoOIV in the winters of 2001/02, 2003/04, 2007/08, and 2010/11, when the intraseasonal SST obtains large amplitudes. The MR has weaker 20–90-day SSTs than NoOIV during the winters of 2002/03, 2006/07, and 2009/10, which are the years with relatively small intraseasonal SST amplitudes. These results indicate that the OIV is an important process that modulates the year-to-year variability of the amplitude of intraseasonal SSTs.

Given the contrasting impacts of OIV in the western and eastern parts of the SCTR, it is instructive to show the 20–90 SSTs separately for the western SCTR

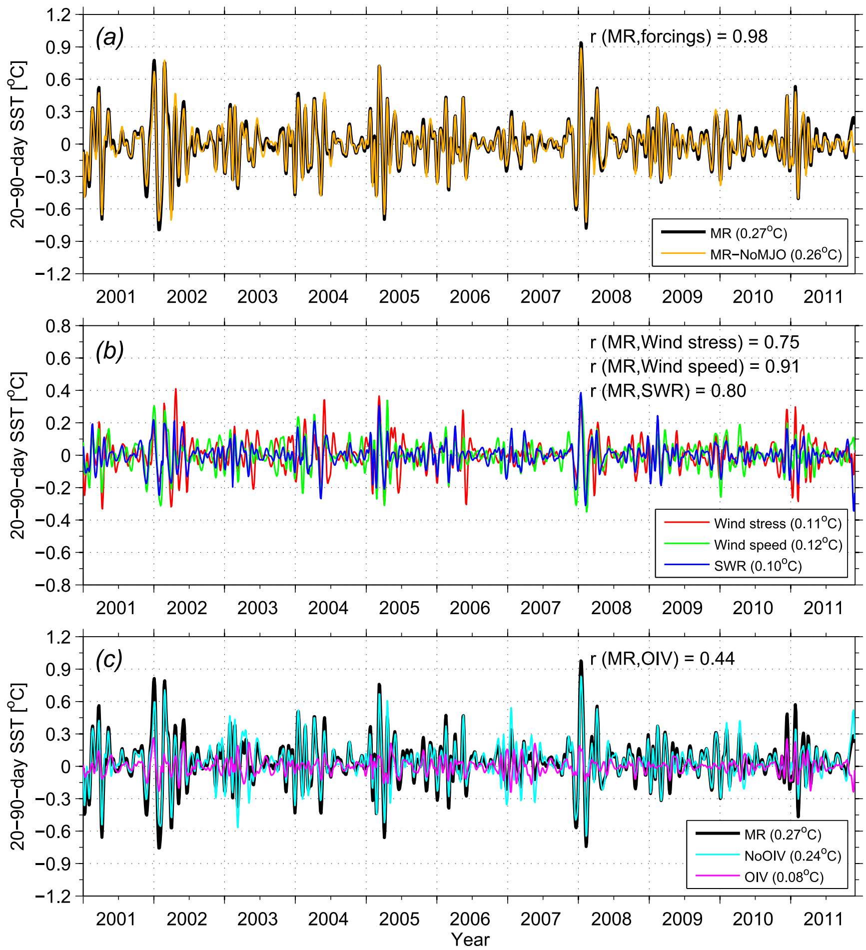

FIG. 4. (a) Time series of the 20–90-day SST (°C) averaged over the SCTR region (12°–4°S, 55°–85°E) from MR (black) and the MR − NoMJO solution (orange; representing the total MJO forcing effect). (b) The 20–90-day SST caused by wind stress (MR − NoSTRESS), wind speed (NoSTRESS − NoWIND), and SWR (MR − NoSWR). (c) The 20–90-day SST from the MR (black), NoOIV (cyan), and the MR − NoOIV solution (pink; representing the OIV effect). Winter STDs of these time series are indicated in the legends.

(SCTR-W; 55°–70°E) and eastern SCTR (SCTR-E; 70°–85°E). In SCTR-W, the difference between MR and NoOIV is very small, with STDs 0.29° versus 0.30°C (Fig. 5a). The OIV effect, in spite of a 0.09°C STD value, has no significant correlation with MR 20–90-day SST (r = 0.06). Figures 5c and 5e compare the SCTR-W 20–90-day SSTs caused by wind stress, wind speed, and SWR with and without the OIV impact. The SST STD induced by wind stress is increased by the OIV from 0.12°C in NoOIV to 0.15°C in MR. Those of the wind speed and SWR effects are, in contrast, reduced from 0.16° and 0.11°C in NoOIV to 0.13° and 0.10°C in the MR, respectively. Also changed are the correlations with the MR variability, with r of the wind stress effect (wind speed and SWR effects) elevated (degraded). These results suggest that in the SCTR-W region, the OIV adjusts the relative importance of the different processes, although its overall impact on the total intraseasonal SSTs is not significant. In the SCTR-E, on the other hand, the OIV effect is much more prominent (Fig. 5b). The STD value in the MR is larger than in NoOIV by 0.06°C, accounting for about 20% of the total intraseasonal SST STD. The OIV effect has 0.12°C STD and is highly correlated with the MR 20–90-day SST (r = 0.66). Figure 5b further reveals that the OIV effect is particularly large for strong events such as those during the winters of 2001/02, 2004/05, 2005/06, and 2010/11. The OIV impact on the wind stress effect is especially large, raising its STD value from 0.07°C in NoOIV to 0.12°C in the MR and increasing its correlation with the MR SST variability from 0.06 in NoOIV to 0.69 in the MR (Figs. 3d,f). Meanwhile, it reduces the wind speed

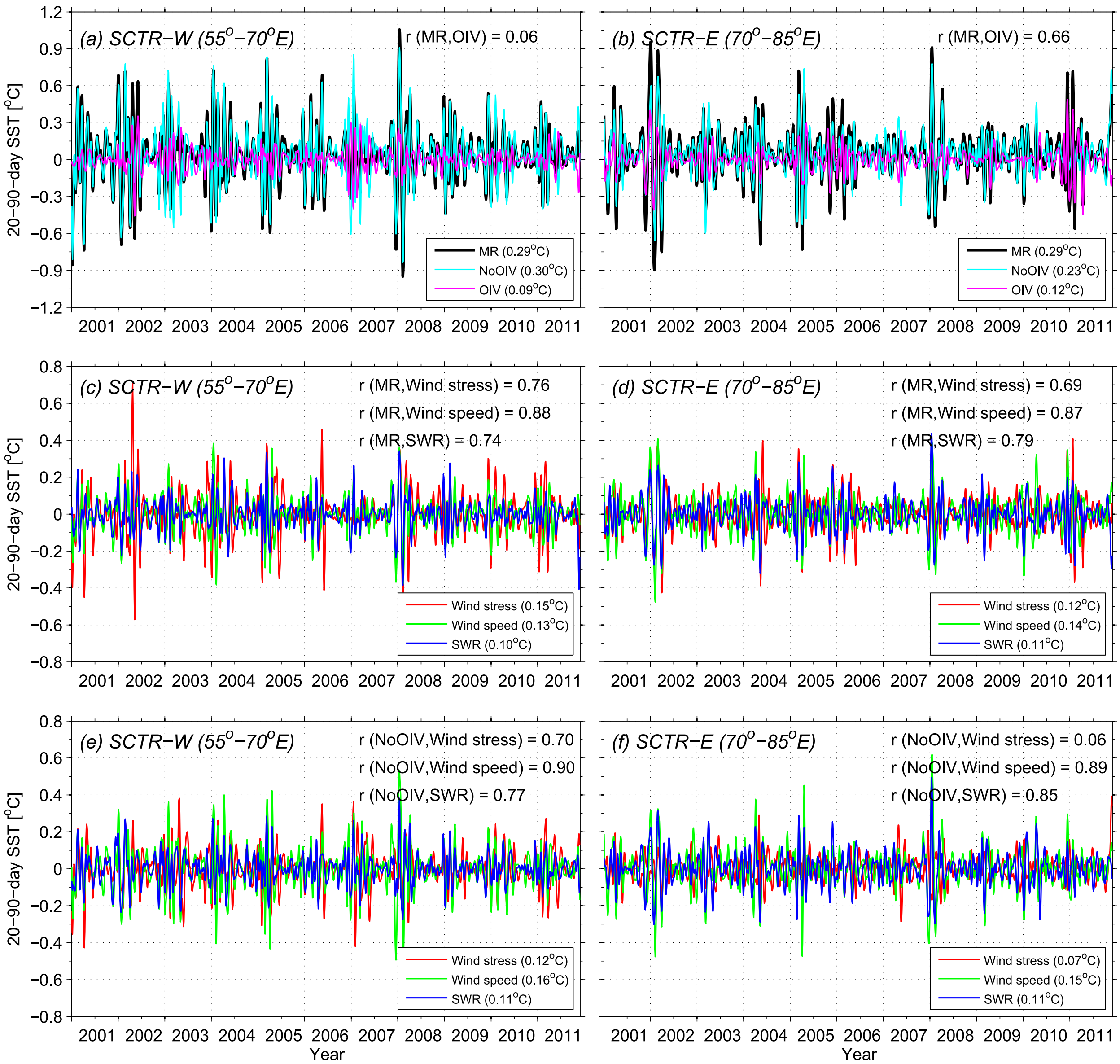

FIG. 5. The 20–90-day SST (°C) from MR (black solid), NoOIV, and the MR − NoOIV solution (the OIV effect) in (a) SCTR-W (55°–70°E) and (b) SCTR-E (70°–85°E). The 20–90-day SST in (c) the SCTR-W and (d) SCTR-E caused by wind stress (MR − NoSTRESS), wind speed (NoSTRESS − NoWIND), and SWR (MR − NoSWR). (e),(f) As in (c) and (d), but estimated from HYCOM experiments without the OIV impact: wind stress (NoOIV − NoOIV_NoSTRESS), wind speed (NoOIV_NoSTRESS − NoOIV_NoWIND), and SWR (NoOIV − NoOIV_NoSWR). Winter STDs of these time series are shown in the legends.

and SWR effects by a small amount. The underlying physics will be discussed in section 3c.

Besides the mean impact during 2001–11, Figs. 4 and 5 also indicate large modulations by the OIV on the year-to-year variability of the amplitude and mechanism of the intraseasonal SSTs. It should be stated that the amplitude of intraseasonal SSTs in the SCTR is also controlled by the strength of the MJO forcing. The all-season real-time multivariate MJO index (RMM) (Wheeler and Hendon 2004) is widely used to identify the large-scale atmospheric variations related to the MJO. Here, we adopt the RMM index from online (http://cawcr.gov.au/staff/mwheeler/maproom/RMM/), which is based on the first two empirical orthogonal functions (EOFs) of the combined fields of near-equator 850- and 200-hPa winds from the National Centers for Environmental Prediction–National Center for Atmospheric Research (NCEP–NCAR) reanalyses (Kalnay et al. 1996) and satellite-observed outgoing longwave radiation (OLR) from the National Oceanic and Atmospheric Administration

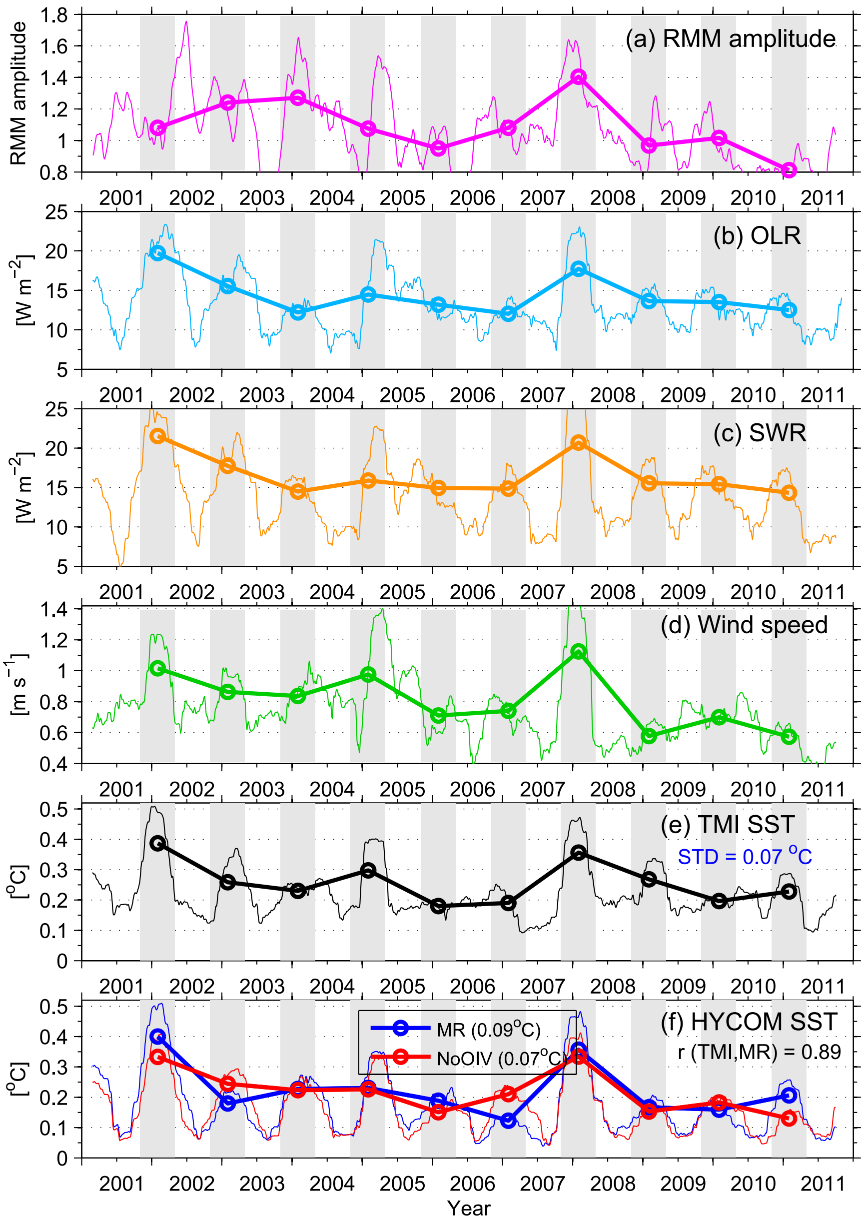

FIG. 6. (a) The 120-day running mean, 20–90-day bandpass-filtered, Wheeler and Hendon (2004) RMM amplitude $(\mathrm{RMM1}^2 + \mathrm{RMM2}^2)^{1/2}$. The 3-day VAR2090 of the SCTR-averaged (b) OLR (W m^{-2}), (c) SWR (W m^{-2}), (d) wind speed (m s^{-1}), (e) SST (°C) from TMI dataset, and (f) SST from MR (blue) and NoOIV (red). The thick dotted curves represent the yearly winter-mean time series, and the gray shadings denote the winters during 2001–11. In (f), the winter STDs of the yearly winter-mean SST VAR2090 are indicated in the legend.

(NOAA) (Liebmann and Smith 1996). Projecting observed atmospheric fields onto the two EOFs yields two principal components, which are defined as the RMM time series 1 (RMM1) and RMM time series 2 (RMM2). For more details of the definition and generating procedures of the RMM index, see Wheeler and Hendon (2004). Here, we use the 120-day running-mean amplitude of the 20–90-day bandpass-filtered RMMs, $(\mathrm{RMM1}^2 + \mathrm{RMM2}^2)^{1/2}$, to quantify the strength of the global-scale atmospheric variability related to the MJO (Fig. 6a).

On the other hand, the strength of regional intraseasonal variability in the SCTR can be quantified by the 120-day running STD of a 20–90-day bandpass-filtered, SCTR-averaged variable $A^{20\text{–}90}$, which we define as a parameter VAR2090:

$$\text{VAR2090} = \text{STD}(A^{20-90}). \tag{4}$$

The intensity of convection perturbations in the SCTR region is hence represented by VAR2090 of OLR (Fig. 6b). Superimposed on an evident seasonal cycle, both the RMM amplitude and the OLR VAR2090 exhibit pronounced year-to-year variability (more evident in the yearly winter-mean time series) with clear consistency. Such accordance indicates that wintertime intraseasonal convection variability in the SCTR is primarily induced by the development or passage of MJO events. The discrepancies between them, such as those in 2001/02 and 2003/04 winters, arise likely from the fact that some of the MJOs are generated in the east Indian–west Pacific warm pool region, while some SCTR-formed MJOs may be greatly diminished before reaching the Pacific Ocean (e.g., Hendon and Glick 1997; Wheeler and Hendon 2004). The VAR2090s of SWR and wind speed show similar interannual modulations (Figs. 6c,d) to that of OLR. This is because variations of surface wind and radiations at 20–90-day periods are predominantly associated with MJO convections. The VAR2090 of SST (Fig. 6e) generally follows the changes of the forcing fields, confirming the dominant role of the MJO forcing in determining the amplitude of the intraseasonal SSTs. These year-to-year changes in SST VAR2090 are also well reproduced by the model (Fig. 6f), with a linear correlation of $r = 0.89$ with TMI satellite data.

Carefully comparing the SST VAR2090 time series with those of the forcing fields reveals some fundamental discrepancies. The forcing fields show low VAR2090 values in 2010/11, but the SST VAR2090 has no minimum in that winter; the simulated SST VAR2090 reaches the minimum in 2006/07, which in turn is absent in the forcing fields. To examine the role of the OIV, we also computed the SST VAR2090 from NoOIV (red curve in Fig. 6f). The OIV tends to strengthen the year-to-year changes of SST VAR2090, increasing the STD value of the yearly winter-meanVAR2090 from 0.07°C in NoOIV to 0.09°C in MR. It evidently enhances the intraseasonal SSTs in 2001/02, 2005/06, and 2010/11 and attenuates them in 2002/03 and 2006/07. Most importantly, the OIV impact can well explain the differences between the observed SST variability and the MJO forcing: it enhances the intraseasonal SSTs in 2010/11 and hence cancels that minimum in SST VAR2090 and reduces the intraseasonal SSTs in 2006/07 by ~40%, which directly leads to the SST VAR2090 minimum in that winter. Besides amplifying the year-to-year difference, the OIV impact can also be an important factor for determining the intraseasonal SST amplitude for some years (recall also Fig. 4).

An additional impact by the OIV is on the year-to-year changes of the relative importance of the wind stress, wind speed, and SWR effects. To quantify such importance, we use the explained variation EV, which is defined as

$$\text{EV} = 1 - \frac{\text{RMS}(\text{Effect}^{20-90} - \text{SST}^{20-90})}{\text{STD}(\text{SST}^{20-90})} \times 100\%, \tag{5}$$

where $\text{Effect}^{20–90}$ is the effect on 20–90-day SST by a forcing variable and its associated processes (e.g., for wind stress, $\text{Effect}^{20–90}$ will be the 20–90-day SST of the MR − NoSTRESS or NoOIV − NoOIV_NoSTRESS solution), RMS denotes the root-mean-square calculation, and $\text{SST}^{20–90}$ is the 20–90-day SST from MR or NoOIV. Similar to VAR2090, the EV is computed within a 120-day running window. In Fig. 7, we compare the EV time series for the effects of wind stress, wind speed, and SWR between cases with (blue) and without (red) the OIV impact. In the 3-day EV time series (thin curves), there is a prominent seasonal cycle. In winter, the MR 20–90-day SST can be well explained by the winds (wind speed plus wind stress) and SWR with large percentage values, whereas in summer EVs of all forcing variables decrease to very low values. This seasonal difference reflects the fact that different from the wintertime case, the summertime intraseasonal SSTs have much weaker association with the MJO forcing and contain significant eddy signals. In winter, wind speed has relatively larger contribution than the other two, with a mean EV value of 39%. The contributions from SWR and wind stress are 31% and 23%.

These estimations generally agree with the STDs and correlations in Fig. 2. It should be noted that due to the nonlinear interaction between the three processes, their EVs cannot add up linearly.

There are discernable year-to-year changes in the winter-mean EV of the wind stress effect (Fig. 7a), which increases to 40% in 2005/06 and 2010/11 and drops to below zero in 2006/07. The OIV impact, indicated by the difference between the red and blue curves, is also larger in the wind stress effect. In most winters, the adjusted wind stress EV by the OIV is at least 10% of the total intraseasonal SSTs. It is interesting that in 9 of the total 10 winters, the OIV acts to enhance the wind stress effect. In 2007/08 and 2010/11, it is increased by more than 30% of the total intraseasonal SSTs. Without the OIV, the contribution of the wind stress will be much smaller (only 11% of the total) than the other two forcing effects. The only exception is the 2006/07 winter, during which the wind stress EV is reduced from ~20% to a negative value by the OIV. The OIV impact on the other two effects is weaker (Figs. 7b,c),

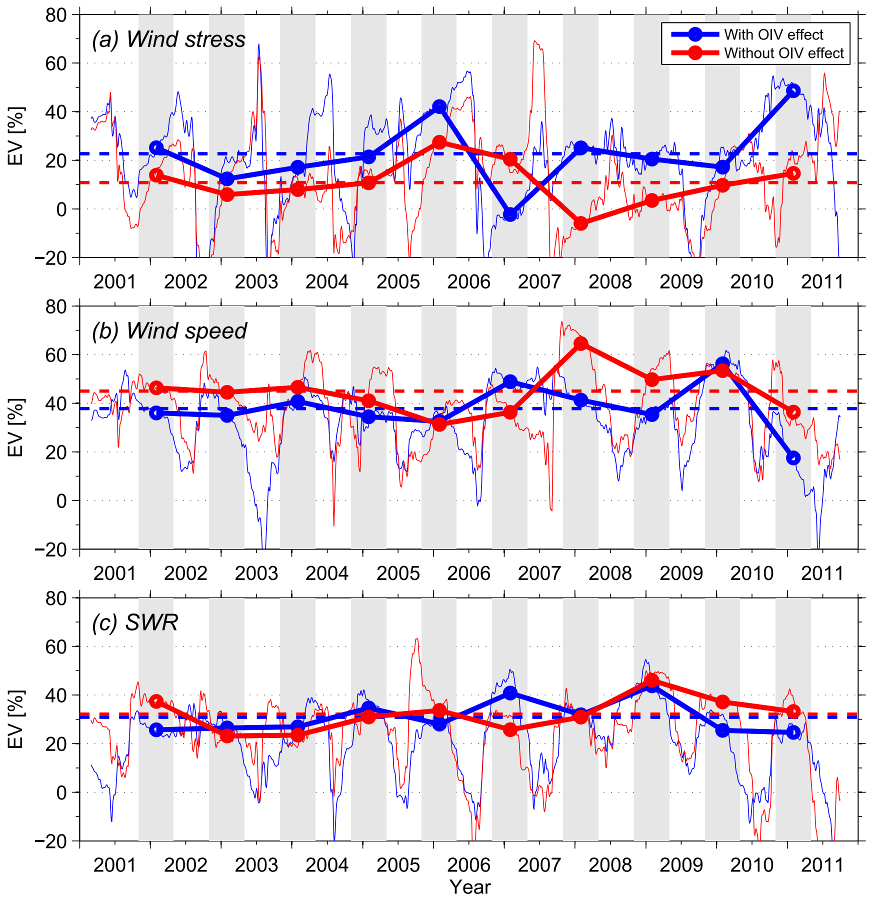

FIG. 7. The blue curves denote the explained variation EV (%) of the SCTR-averaged MR 20–90-day SST by (a) wind stress effect (MR − NoSTRESS), (b) wind speed effect (NoSTRESS − NoWIND), and (c) SWR effect (MR − NoSWR), while the red curves are those estimated using HYCOM experiments without the OIV impact: NoOIV and NoOIV − NoOIV_NoSTRESS in (a), NoOIV and MoOIV_NoSTRESS − NoOIV_NoWIND in (b), and NoOIV and NoOIV − NoOIV_NoSWR in (c). The thin curves denote the original 3-day EV time series, while the thick dotted curves denote the yearly winter-mean time series. The dashed straight lines denote the mean values during the model period.

which is consistent with the results in Fig. 5. The heat flux effect (wind speed plus SWR) is significantly strengthened in 2006/07 and suppressed in 2007/08 and 2010/11. Because the EV measures the "relative" contribution of an effect, such changes are, to a large degree, also attributed to the changes in wind stress effect. When the wind stress effect is increased (decreased) by the OIV, the contribution of heat fluxes will be automatically decreased (increased). In general, our results have demonstrated that the OIV is a critical factor modulating the relative importance of wind stress–driven upper-ocean processes versus heat flux forcing.

c. Processes

In this section, we examine the processes through which the OIV influences the MJO SST signature. The covariability of SST, MLD, and Z_{20} shown in Fig. 2 suggests the reasonability of using Z_{20} as an index representing the ocean state of the SCTR region. We categorize the 10 winters during 2001–11 into three groups: the weak SCTR, strong SCTR, and medium situations. A weak SCTR winter has a deeper-than-normal thermocline and thus a weaker thermocline ridge (Tozuka et al. 2010). This group consists of the 2002/03, 2004/05, 2006/07, and 2009/10 winters, with the winter-mean MR Z_{20} deeper than that of NoOIV by at least 4 m (accounting for ~40% of the STD value of the yearly winter-mean Z_{20} time series) (Fig. 2c). In three out of four of these weak SCTR winters, the SST VAR2090 is decreased by the OIV (Fig. 6f). The strong SCTR group, with the winter-mean MR Z_{20} shallower by at least 4 m, consists of the 2001/02, 2005/06, 2007/08, and 2010/11

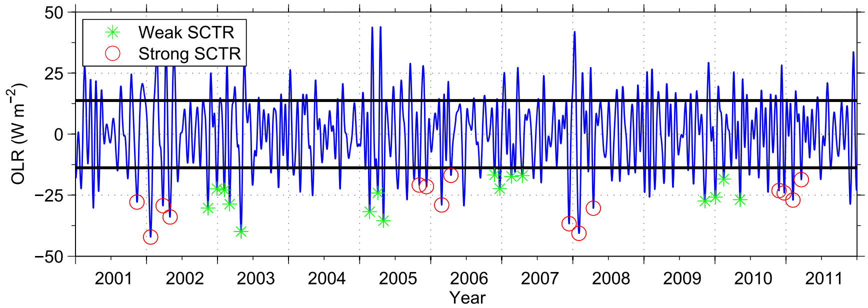

FIG. 8. The 20–90-day OLR (W m^{-2}) averaged over the SCTR. The black straight lines indicate one STD value range, and the green asterisks (red circles) mark the OLR minima with magnitudes exceeding one STD value in weak (strong) SCTR winters.

winters. These strong SCTRs all act to enhance the intraseasonal SSTs (Fig. 6f). The remaining two winters, 2003/04 and 2008/09, belong to the medium group, during which the intraseasonal SSTs are in fact also enhanced by a small amount. Another definition of thermocline depth, depth of the 23°C isotherm, is also used to test the stability of strong/weak categorization. When using Z_{23}, the only change is for the 2008/09 winter, which will be moved from the medium group to the strong SCTR group. To explore the mechanism of the OIV affecting intraseasonal mixed layer variations, we should assess the difference between the weak SCTR and strong SCTR cases. We therefore perform a composite analysis for MJO events based on the SCTR-averaged 20–90-day OLR value. There are respectively 16 and 15 wintertime convection events with 20–90-day OLR reaching minima and exceeding one STD magnitude during the weak SCTR and strong SCTR winters (Fig. 8), which are used to construct the weak SCTR and strong SCTR composite MJOs, respectively. The days with OLR minima are taken as the 0-day phase, representing the wet (active) peak of a MJO event. Then, a 41-day composite MJO event is produced by simply averaging variables for each time step between the −20 day and +20 day.

Because the OIV impact is statistically significant only in the SCTR-E (70°–85°E) region (Fig. 3d), we only examine the composite for that subregion. The variation of OLR is the reference for identifying different stages of a composite MJO (Fig. 9a). OLR shows two maxima at around the −14 day and +14 day, marking the calm (inactive) stages of pre- and postconvection conditions. The periods of the −14 ~ 0 day and 0 ~ +14 day are the developing and decaying stages, respectively. The SST tendency, $\mathrm{SST}_t = \partial\mathrm{SST}/\partial t$, achieves minimum between the −5 day and +2 day (Fig. 9b), indicating the largest cooling effect during this period. The evolution of SST_t is such that SST minimum occurs at around the +5 ~ +6 day, lagging behind the convection peak (OLR minimum) by approximately a ¼ cycle (e.g., Hendon and Glick 1997; Woolnough et al. 2000). The OIV impact exists mainly on the cooling period, suppressing (enhancing) it under the weak SCTR (strong SCTR) condition. In the weak SCTR case, the cooling between −10 ~ 0 day is weaker in the MR than in NoOIV by about 2×10^{-7} °C s^{-1}, whereas in the strong SCTR case it is stronger by about 4×10^{-7} °C s^{-1}. In addition, the OIV also acts to enhance the calm-stage warming of SST in the strong SCTR case, which further contributes to the strengthening of the intraseasonal SSTs, whereas in the weak SCTR case the MR/NoOIV difference is small at the calm stage. The strong–weak difference of SST_t (Fig. 9b, right) is significant at the 90% confidence level in both the precondition calm/warming stage and the wet/cooling stage, suggesting systematic impact of the OIV on the SST evolution during the MJO events. The large strengthening effect in the strong SCTR case and relatively small weakening effect in the weak SCTR case implies the asymmetric impact of the OIV on SST_t between the weak and strong SCTR conditions, which leads to an overall strengthening effect on SST_t (recall Figs. 3d and 5b).

As we shall see below, such asymmetry arises from the nonlinearity of the underlying processes. Because of the different impacts of the OIV on heat flux and wind stress effects (Figs. 5 and 7), we examine them separately. The heat flux forcing HF on the mixed layer can be roughly estimated by $\mathrm{HF} = (\sigma c_p)^{-1}Q/H$, where Q is the net total surface heat flux, σ and c_p are the density and specific heat of seawater, and H is MLD. Here, we obtain Q directly from the model output and ignore the penetrating of SWR below the mixed layer. Similar to SST_t, the MR/NoOIV difference of HF is very small in the weak SCTR composite but large in the strong SCTR composite (Fig. 9c), suggesting that HF is an important source of the asymmetry in the SST_t. In Fig. 10, we will show that this is primarily due to the difference in MLD. A thick (thin) MLD in a weak (strong) SCTR winter

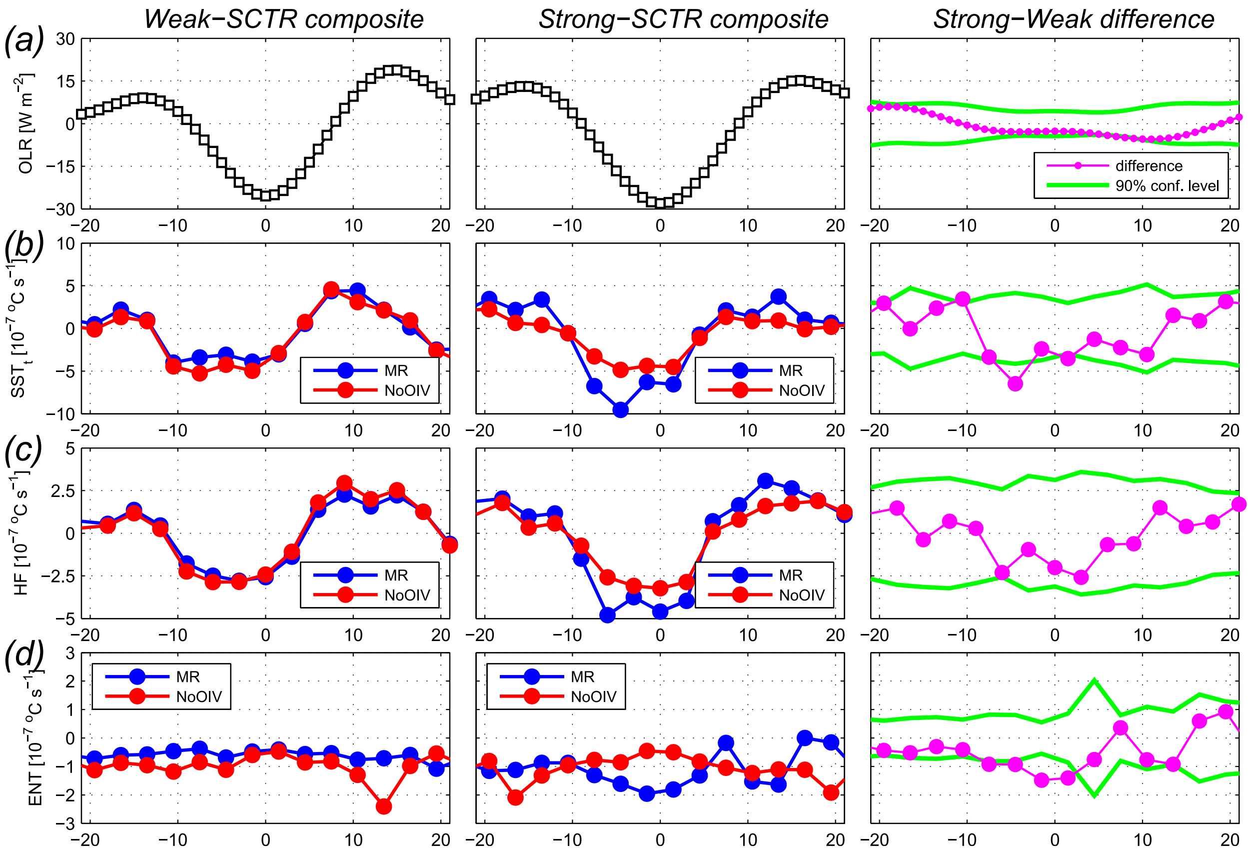

FIG. 9. Evolutions of (a) 20–90-day OLR (black; W m^{-2}), (b) SST tendency SST$_t$ (10^{-7}°C s^{-1}), (c) total heat flux forcing HF (10^{-7}°C s^{-1}; mean values removed), and (d) entrainment cooling ENT (10^{-7}°C s^{-1}) of the weak SCTR (left) and strong SCTR (middle) composite MJO events. In (b)–(d) blue (red) curves denote the results from MR (NoOIV). The difference (pink dotted) between the weak and strong SCTR composites (strong minus weak), in which the green curves denote the 90% confidence level interval determined by a two-tailed Student's t test are given (right). All the variables are averaged in the SCTR-E region (70°–85°E).

causes weaker (stronger) SST responses to MJO heat flux forcing. But because of the nonlinear nature of the MLD formation, the thinning in the strong SCTR years is much more evident than the thickening in the weak SCTR years (Fig. 10c).

Comparing the peak-to-peak differences suggests that the strong–weak difference of HF (Fig. 9c, right) is only half of that of SST$_t$ (note that the value ranges in Figs. 9b and 9c are different) and not statistically significant throughout the composite MJO event, implying that HF is not the only source of the asymmetry. Figure 7 indicates that the OIV impact is much larger on the wind stress effect than on SWR and wind speed effects. Wind stress–driven upper-ocean processes include advection, upwelling, and entrainment. Previous observational and modeling studies demonstrated that, although lateral advection is not negligible in the SCTR region, its correlation with the MJO SST signature is small and hence contributes weakly to the intraseasonal mixed layer heat budget (e.g., Vialard et al. 2008; Jayakumar et al. 2011). On the other hand, the upwelling term, if roughly calculated as Ekman pumping EP $= -w_E \partial T/\partial z$, where $w_E = \mathrm{curl}(\tau/f)\sigma_o^{-1}$ is the Ekman pumping velocity (f is the Coriolis parameter; $\sigma_o = 1022\,\mathrm{kg\,m^{-3}}$ is the mean seawater density of the Ekman layer) and $\partial T/\partial z$ is the vertical temperature gradient at MLD, is at least one order smaller than SST$_t$ in magnitude (not shown). Then, we assess the entrainment term, which is suggested to be an important process for the MJO-forced SST variability by observational studies (e.g., Vinayachandran and Saji 2008; McPhaden and Foltz 2013). Here, the entrainment term ENT is calculated as

$$\mathrm{ENT} = -\frac{\partial H}{\partial t}\frac{\Delta T}{H}h^*, \tag{6}$$

where h^* is a Heaviside function, which equals zero for a shoaling mixed layer ($\partial H/\partial t < 0$) and equals 1 for a deepening mixed layer ($\partial H/\partial t > 0$), and ΔT is the temperature difference between the mixed layer and

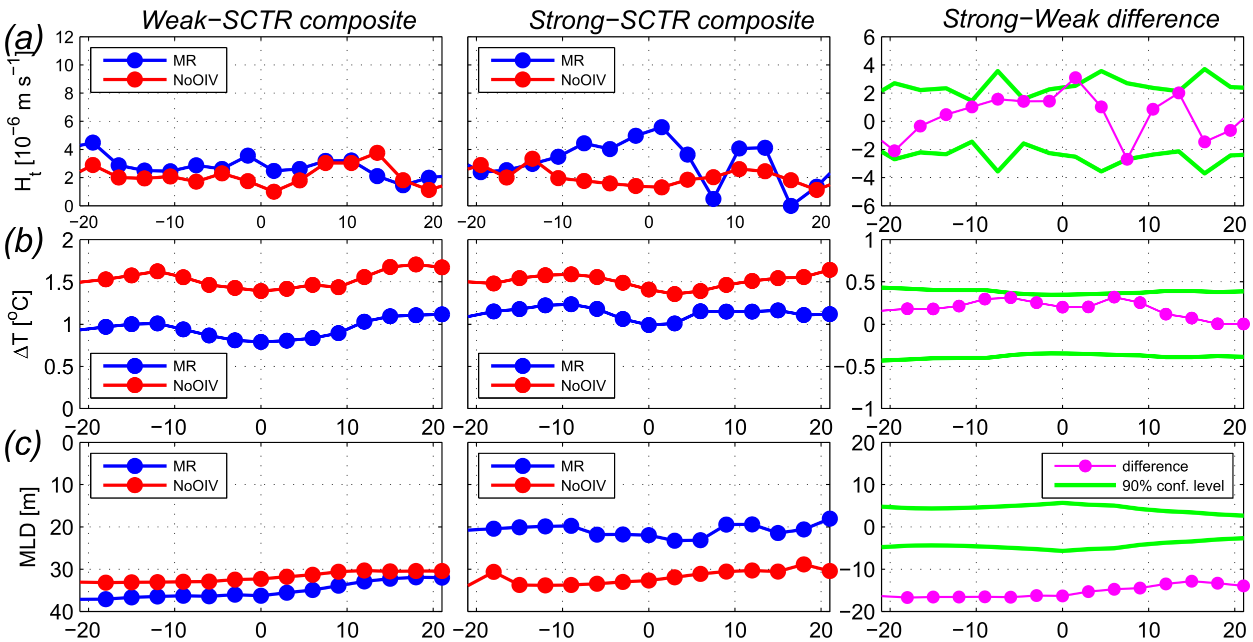

FIG. 10. Evolutions of (a) MLD tendency H_t (10^{-6} m s^{-1}), (b) temperature difference ΔT (°C) between the mixed layer and the water 10 m below, and (c) MLD (m) of the (left) weak SCTR and (middle) strong SCTR composite MJO events. For each time step, H_t, ΔT, and MLD are averaged only over grid points with deepening MLDs ($H_t > 0$). In (b)–(c) blue (red) curves denote the results from MR (NoOIV). (right) The difference (pink dotted) between the weak and strong SCTR composites (strong minus weak), in which the green curves denote the 90% confidence level interval determined by a two-tailed Student's t test. All the variables are averaged in the SCTR-E region (70°–85°E).

10 m below. Altering the depth difference to 5 or 8 m causes no significant changes in ENT. The MR ENT averaged over the SCTR-E region is smaller than the NoOIV ENT under the weak SCTR condition by about 0.3×10^{-7} °C s^{-1} (Fig. 11d), whereas under the strong SCTR condition the difference between the two exceeds 1.5×10^{-7} °C s^{-1} during the cooling stage (Fig. 9d). The MR/NoOIV difference is also significant during that stage (Fig. 9d, right). The residual ENT value between strong and weak SCTR cases is probably one of the major sources of the asymmetric impact on SST$_t$ by the OIV.

For a more in-depth understanding of the ENT term, we display in Fig. 10 all the factors in it [Eq. (6)], including the MLD tendency $H_t = \partial H/\partial t$, the temperature difference ΔT, and MLD H averaged over the SCTR-E. As the westerly wind develops with the MJO convection in the SCTR region (e.g., Han et al. 2007; Li et al. 2013; Shinoda et al. 2013), the MLD deepens in response to the wind speed increase. The deepening rate H_t is clearly larger during the wet/cooling stage of the strong SCTR composite MJO (Fig. 10a). The strong–weak difference is small and not significant in ΔT (Fig. 10b). Such difference is most evident in MLD H; while a weak SCTR thickens the mean MLD by less than 4 m, a strong SCTR can lift the mean MLD upward by more than 10 m. The smaller-mean MLD in the strong SCTR years favors a larger deepening rate H_t in response to strong winds of MJO and is also the reason for the enlarged HF term (Fig. 9c). Because of the smaller MLD and larger H_t, the resultant ENT term is greatly enlarged at the cooling stage of the strong SCTR composite MJO (Fig. 9d).

The analysis presented in this subsection provides quantitative estimates and insights into the complicated processes through which the OIV imposes asymmetric effects on the intraseasonal SST variability between the strong and weak SCTR conditions. It is demonstrated that such asymmetry is deeply rooted in the nonlinear nature of the upper-ocean thermal stratification. To better interpret this point, we compare in Fig. 11 the mean vertical temperature sections between the weak and strong SCTR years. The difference of MLD is much larger in the SCTR-E than in the SCTR-W, which is the primary reason for the contrasting OIV impacts on the two parts. The related upper-ocean processes, such as entrainment, are also highly nonlinear. They may become even more elusive when interactions between different time scales and different forcing processes are considered as in this study. These results suggest that the intraseasonal SST variability in the SCTR region is far from a linear slab ocean response to the MJO's surface flux changes.

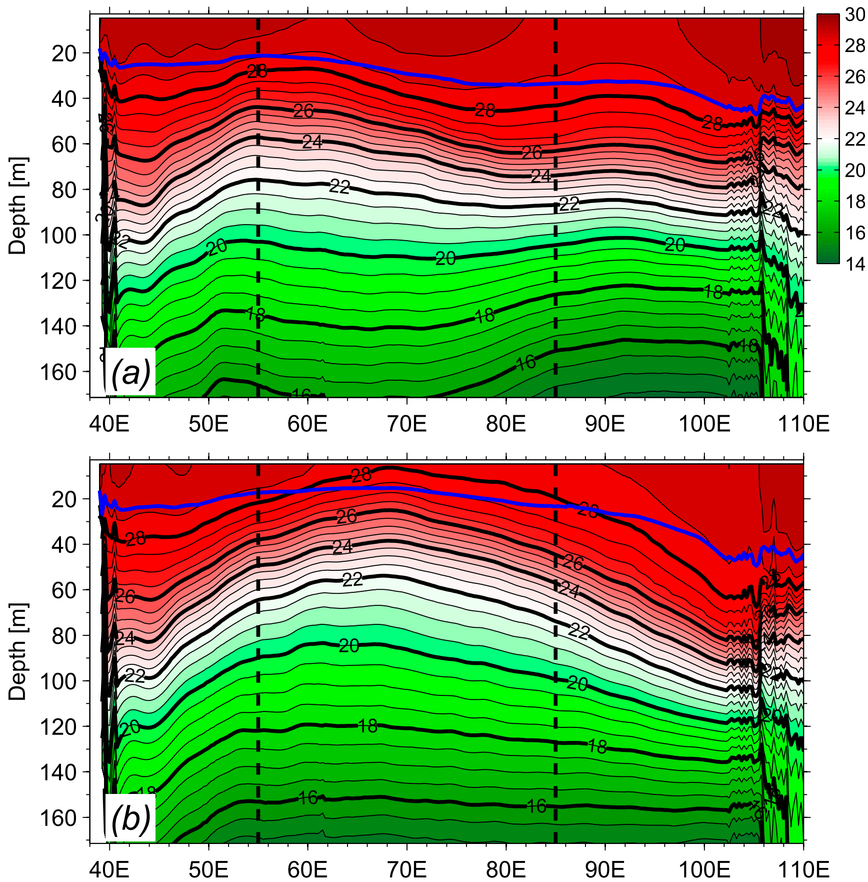

FIG. 11. Zonal–vertical sections of mean winter temperature (°C) from MR averaged between the latitude range of the SCTR (12°–4°S) for (a) weak and (b) strong SCTR years. The blue curves denote the mean MLD, and the dashed straight lines remark the longitude range of the SCTR.

4. Summary and discussion

Intraseasonal SST variability in the SCTR region is drawing increasing attention because of its potential importance in the initiation of wintertime MJO events (e.g., Saji et al. 2006; Bellenger et al. 2009; Izumo et al. 2010; Webber et al. 2012a). In this study, we revisit the processes controlling the wintertime intraseasonal variability associated with the MJO in this region using a series of HYCOM experiments. Recently available, high-quality satellite atmospheric datasets are used as the forcing fields, and model configurations are adjusted to better isolate effects of different processes, which improve the ability of the model in presenting the upper-ocean processes associated with the MJO SST signature. The focus of this study is the impact of OIV on the intraseasonal SSTs. Such an impact and underlying physics are systematically investigated, and the findings are summarized as follows:

1) The large-scale 20–90-day SST variation in the SCTR region (12°–4°S, 55°–85°E) in boreal winter is predominantly induced by atmospheric forcing of the MJO. Through a series of experiments isolating different effects, we find that three primary factors, wind stress–driven ocean dynamics, wind speed–controlled surface turbulent heat fluxes, and SWR, are all important in causing the intraseasonal SSTs. During the 2001–11 model period, the contribution of the wind speed effect is relatively larger (39%) compared with SWR (31%) and wind stress (23%) effects.
2) Through OGCM experiments removing the OIV, the OIV impacts on the intraseasonal SSTs are assessed. Averaged over the entire SCTR region, the OIV generally acts to strengthen the intraseasonal SST variability. Such impact has an interesting spatial pattern, with the intraseasonal SSTs in the eastern part (70°–85°E) enhanced by >20%, which is significant at the 95% confidence level, and those in the western part (55°–70°E) nonsignificantly suppressed by ~3%.
3) The OIV also adjusts the relative importance of different factors. During the modeling period of

2001–11, the OIV generally enhances the wind stress effect and slightly reduces the heat flux forcing effect (wind speed plus SWR).

4) Besides the strength of the MJO forcing, the OIV is another important factor modulating the year-to-year changes of the intraseasonal SST amplitude. The STD of the yearly winter-mean amplitude of the intraseasonal SSTs (quantified by the SST VAR2090) is raised from 0.07°C in NoOIV to 0.09°C in MR. A stronger (weaker) SCTR favors a larger (smaller) MJO SST signature.
5) The year-to-year variation of mechanism, that is, the relative importance of the three factors, is also largely modulated. Such influence is mainly imposed on the wind stress effect. In most (9 out of 10) of the simulated winters, the wind stress contribution is at least raised by 5% of the total SST variability. In the 2005/06 and 2010/11 winters, it is increased by ~30%, whereas in the 2006/07 winter, it is decreased by >20%.
6) The processes through which the OIV affects the intraseasonal SST variability are further explored through a composite analysis. Intraseasonal SST variability shows an evident asymmetry between the weak (deep thermocline) and strong (shallow thermocline) SCTR cases. In the SCTR-E region, where the OIV impact is significant, both the heat flux forcing and entrainment cooling terms are greatly amplified by a strong SCTR but only moderately changed by a weak SCTR, leaving behind an overall enhancing effect by the OIV on the intraseasonal SSTs.
7) It is further demonstrated that the nonlinear nature of the upper-ocean thermal stratification, such as MLD changes, are the major source for the asymmetry of the intraseasonal SST variability between the strong and weak SCTR cases.

The conclusions reached here deviate from previous studies in a quantitative sense. Han et al. (2007) showed that winds are the dominant forcing for the 30–90-day SSTs, and SWR generally plays a minor role with the maximum contribution of 20%. Their wind forcing contains both wind speed and wind stress effects. In our result, the total wind forcing effect (MR − NoWIND) accounts for 74% of the total variability, which confirms the dominant role of wind forcing, although our estimated SWR effect is larger (31%). Another important modeling work, Jayakumar et al. (2011), suggested a total contribution of 70% by the heat flux forcing, in which SWR is the major contributor (75%), dominating over the other flux component (25%), and the contribution of wind stress is only about 20%. Our estimation suggests a smaller SWR contribution (31% vs 52.5%) and a larger wind stress contribution (23% vs 20%). These discrepancies with previous studies may arise from various sources in the model settings. With the advanced forcing fields and higher model resolution, our model achieves more favorable comparisons with the satellite/in situ observations (Figs. 1–3). The relative importance of individual factors estimated in this study may be closer to the reality.

Our results are based on the 11-yr model simulation, which is more or less short in assessing the impact of the OIV. An investigation using longer experiments (e.g., ~30 yr) will be helpful to confirm our findings. In addition, as one of the reviewers has pointed out, our estimations for the heat flux forcing and entrainment using 3-day model outputs are rather coarse, and a comprehensive mixed layer heat budget analysis using daily or higher-resolution model output (e.g., Wang et al. 2012b) can upgrade the work. With the rapid development of numerical models and accumulation of the high-quality satellite observation, these issues should be further examined in the future.

Because of the tight coupling between the mixed layer thermal variability and subsurface ocean dynamics, the thermocline depth (i.e., Z_{20}) is a key variable representing the mean ocean state and modulating the intraseasonal SST variability in the SCTR region. Interannual variations of Z_{20} are believed to be associated with both the ENSO and IOD modes through mainly ocean baroclinic wave adjustments (e.g., Masumoto and Meyers 1998; Xie et al. 2002; Tozuka et al. 2010; Yokoi et al. 2012). The yearly time series of the September–November (SON) dipole mode index (DMI) (Rao and Behera 2005) and December–February (DJF) Niño-3.4 index during the modeled period are shown in Fig. 12. The interannual variation of winter Z_{20} in the SCTR has significant correlation (r = 0.71 and 0.85) with both. Calculation with monthly, low-pass-filtered data yields similar results but with time lags of 0–3 months. Such a relationship is generally consistent with these previous studies. There is also an interesting relationship with a strong SCTR year followed by a weak SCTR year, especially during 2002–07. This may be related to the tropospheric biennial oscillation (TBO) (Meehl 1997; Meehl and Arblaster 2002) in the tropical Indo-Pacific region or the biennality of the IOD (e.g., Meehl et al. 2003; Behera et al. 2005). The OIV associated with those climate modes can influence not only the forced intraseasonal SSTs but also their feedbacks to the atmosphere through surface turbulent heat fluxes. Such an effect in the initiation area for the wintertime MJOs may contribute to their interannual variability in their activity and spatial–temporal features. Although interannual

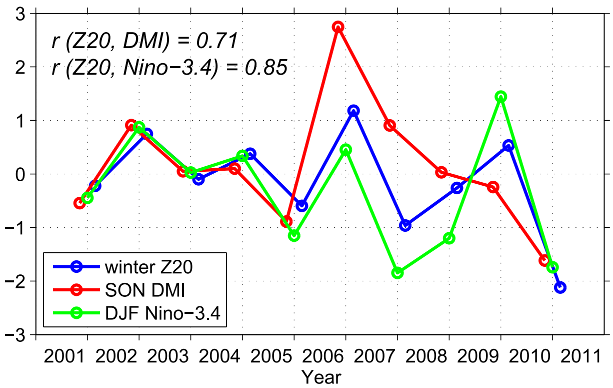

FIG. 12. Yearly winter-mean time series of MR Z_{20} in the SCTR (blue), the SON-mean DMI (red), and the DJF-mean Niño-3.4 index (green). All the variables are normalized to achieve better comparison. The DMI data are adopted from the Frontier Research Center for Global Change of the Japan Agency for Marine-Earth Science and Technology (JAMSTEC), and the Niño-3.4 index is taken from the Climate Prediction Center (CPC) of NOAA.

modulations of the MJO by the ENSO and IOD have been reported by several studies (e.g., Hendon et al. 1999; Shinoda and Han 2005; Pohl and Matthews 2007; Ito and Satomura 2009; Izumo et al. 2010), it is still difficult to explain them from a purely atmospheric point of view. Alternatively, the large OIV impact on intraseasonal SST variability revealed in this study proposes a linkage between the interannual climate modes and MJOs through the ocean.

Acknowledgments. Y. Li and W. Han are supported by NOAA NA11OAR4310100 and NSF CAREER Award 0847605. Insightful comments and suggestions from two anonymous reviewers and the editor Dr. William Kessler are very helpful in improving our work. This work also benefits from the discussion with Dr. Michael McPhaden. We appreciate the help from Office of Information Technology (OIT) of University of Colorado in maintaining the computational resources. We thank Allan Wallcraft for the technical consultation on HYCOM model.

REFERENCES

Annamalai, H., P. Liu, and S.-P. Xie, 2005: Southwest Indian Ocean SST variability: Its local effect and remote influence on Asian monsoons. *J. Climate,* **18,** 4150–4167, doi:10.1175/JCLI3533.1.

——, H. Okajima, and M. Watanabe, 2007: Possible impact of the Indian Ocean SST on the Northern Hemisphere circulation during El Niño. *J. Climate,* **20,** 3164–3189, doi:10.1175/JCLI4156.1.

Antonov, J. I., and Coauthors, 2010: *Salinity.* Vol. 2, *World Ocean Atlas 2009,* NOAA Atlas NESDIS 69, 184 pp.

Atlas, R., J. Ardizzone, and R. N. Hoffman, 2008: Application of satellite surface wind data to ocean wind analysis. *Remote Sensing System Engineering,* P. E. Ardanuy and J. J. Puschell, Eds., International Society for Optical Engineering (SPIE Proceedings 7087), 70870B, doi:10.1117/12.795371.

Behera, S. K., J.-J. Luo, S. Masson, P. Delecluse, S. Gualdi, A. Navarra, and T. Yamagata, 2005: Paramount impact of the Indian Ocean dipole on the East African short rains: A CGCM study. *J. Climate,* **18,** 4514–4530, doi:10.1175/JCLI3541.1.

Bellenger, H., J. P. Duvel, M. Lengaigne, and P. Levan, 2009: Impact of organized intraseasonal convective perturbations on the tropical circulation. *Geophys. Res. Lett.,* **36,** L16703, doi:10.1029/2009GL039584.

Bernie, D., S. Woolnough, J. Slingo, and E. Guilyardi, 2005: Modeling diurnal and intraseasonal variability of the ocean mixed layer. *J. Climate,* **18,** 1190–1202, doi:10.1175/JCLI3319.1.

——, E. Guilyardi, G. Madec, J. Slingo, and S. Woolnough, 2007: Impact of resolving the diurnal cycle in an ocean–atmosphere GCM. Part 1: A diurnally forced OGCM. *Climate Dyn.,* **29,** 575–590, doi:10.1007/s00382-007-0249-6.

Bleck, R., 2002: An oceanic general circulation model framed in hybrid isopycnic-Cartesian coordinates. *Ocean Modell.,* **4,** 55–88, doi:10.1016/S1463-5003(01)00012-9.

Bretherton, C. S., M. Widmann, V. P. Dymnikov, J. M. Wallace, and I. Blade, 1999: The effective number of spatial degrees of freedom of a time-varying field. *J. Climate,* **12,** 1990–2009, doi:10.1175/1520-0442(1999)012<1990:TENOSD>2.0.CO;2.

Dai, A., T. Qian, K. E. Trenberth, and J. D. Milliman, 2009: Changes in continental freshwater discharge from 1948 to 2004. *J. Climate,* **22,** 2773–2792, doi:10.1175/2008JCLI2592.1.

de Boyer Montégut, C., G. Madec, A. S. Fischer, A. Lazar, and D. Iudicone, 2004: Mixed layer depth over the global ocean: An examination of profile data and a profile-based climatology. *J. Geophys. Res.,* **109,** C12003, doi:10.1029/2004JC002378.

Dee, D., and Coauthors, 2011: The ERA-Interim reanalysis: Configuration and performance of the data assimilation system. *Quart. J. Roy. Meteor. Soc.,* **137,** 553–597, doi:10.1002/qj.828.

Duchon, C. E., 1979: Lanczos filtering in one and two dimensions. *J. Appl. Meteor.,* **18,** 1016–1022, doi:10.1175/1520-0450(1979)018<1016:LFIOAT>2.0.CO;2.

Duncan, B., and W. Han, 2009: Indian Ocean intraseasonal sea surface temperature variability during boreal summer: Madden–Julian oscillation versus submonthly forcing and processes. *J. Geophys. Res.,* **114,** C05002, doi:10.1029/2008JC004958.

——, and ——, 2012: Influence of atmospheric intraseasonal oscillations on seasonal and interannual variability in the upper Indian Ocean. *J. Geophys. Res.,* **117,** C11028, doi:10.1029/2012JC008190.

Duvel, J. P., and J. Vialard, 2007: Indo-Pacific sea surface temperature perturbations associated with intraseasonal oscillations of tropical convection. *J. Climate,* **20,** 3056–3082, doi:10.1175/JCLI4144.1.

——, R. Roca, and J. Vialard, 2004: Ocean mixed layer temperature variations induced by intraseasonal convective perturbations over the Indian Ocean. *J. Atmos. Sci.,* **61,** 1004–1023, doi:10.1175/1520-0469(2004)061<1004:OMLTVI>2.0.CO;2.

Fairall, C., E. F. Bradley, J. Hare, A. Grachev, and J. Edson, 2003: Bulk parameterization of air–sea fluxes: Updates and verification for the COARE algorithm. *J. Climate,* **16,** 571–591, doi:10.1175/1520-0442(2003)016<0571:BPOASF>2.0.CO;2.

Flatau, M., P. J. Flatau, P. Phoebus, and P. P. Niiler, 1997: The feedback between equatorial convection and local radiative and evaporative processes: The implications for intraseasonal oscillations. *J. Atmos. Sci.,* **54,** 2373–2386, doi:10.1175/1520-0469(1997)054<2373:TFBECA>2.0.CO;2.

Gadgil, S., P. V. Joseph, and N. V. Joshi, 1984: Ocean-atmosphere coupling over monsoon regions. *Nature,* **312,** 141–143, doi:10.1038/312141a0.

Han, W., and J. P. McCreary, 2001: Modeling salinity distributions in the Indian Ocean. *J. Geophys. Res.,* **106,** 859–877, doi:10.1029/2000JC000316.

——, P. Webster, R. Lukas, P. Hacker, and A. Hu, 2004: Impact of atmospheric intraseasonal variability in the Indian Ocean: Low-frequency rectification in equatorial surface current and transport. *J. Phys. Oceanogr.,* **34,** 1350–1372, doi:10.1175/1520-0485(2004)034<1350:IOAIVI>2.0.CO;2.

——, T. Shinoda, L. L. Fu, and J. P. McCreary, 2006: Impact of atmospheric intraseasonal oscillations on the Indian Ocean dipole during the 1990s. *J. Phys. Oceanogr.,* **36,** 670–690, doi:10.1175/JPO2892.1.

——, D. Yuan, W. T. Liu, and D. Halkides, 2007: Intraseasonal variability of Indian Ocean sea surface temperature during boreal winter: Madden–Julian oscillation versus submonthly forcing and processes. *J. Geophys. Res.,* **112,** C04001, doi:10.1029/2006JC003791.

Harrison, D. E., and G. A. Vecchi, 2001: January 1999 Indian Ocean cooling event. *Geophys. Res. Lett.,* **28,** 3717–3720, doi:10.1029/2001GL013506.

Hendon, H. H., 2000: Impact of air–sea coupling on the Madden–Julian oscillation in a general circulation model. *J. Atmos. Sci.,* **57,** 3939–3952, doi:10.1175/1520-0469(2001)058<3939:IOASCO>2.0.CO;2.

——, and J. Glick, 1997: Intraseasonal air–sea interaction in the tropical Indian and Pacific Oceans. *J. Climate,* **10,** 647–661, doi:10.1175/1520-0442(1997)010<0647:IASIIT>2.0.CO;2.

——, C. Zhang, and J. D. Glick, 1999: Interannual variation of the Madden–Julian oscillation during austral summer. *J. Climate,* **12,** 2538–2550, doi:10.1175/1520-0442(1999)012<2538:IVOTMJ>2.0.CO;2.

Hermes, J. C., and C. J. C. Reason, 2008: Annual cycle of the south Indian Ocean (Seychelles-Chagos) thermocline ridge in a regional ocean model. *J. Geophys. Res.,* **113,** C04035, doi:10.1029/2007JC004363.

Hosoda, S., T. Ohira, and T. Nakamura, 2008: A monthly mean dataset of global oceanic temperature and salinity derived from Argo float observations. *JAMSTEC Rep. Res. Dev.,* **8,** 47–59, doi:10.5918/jamstecr.8.47.

Hung, M.-P., J.-L. Lin, W. Wang, D. Kim, T. Shinoda, and S. J. Weaver, 2013: MJO and convectively coupled equatorial waves simulated by CMIP5 climate models. *J. Climate,* **26,** 6185–6214, doi:10.1175/JCLI-D-12-00541.1.

Inness, P. M., and J. M. Slingo, 2003: Simulation of the Madden–Julian oscillation in a coupled general circulation model. Part I: Comparison with observations and an atmosphere-only GCM. *J. Climate,* **16,** 345–364, doi:10.1175/1520-0442(2003)016<0345:SOTMJO>2.0.CO;2.

——, ——, E. Guilyardi, and J. Cole, 2003: Simulation of the Madden–Julian oscillation in a coupled general circulation model. Part II: The role of the basic state. *J. Climate,* **16,** 365–382, doi:10.1175/1520-0442(2003)016<0365:SOTMJO>2.0.CO;2.

Ito, M., and T. Satomura, 2009: The interannual variation of intraseasonal oscillation linked with the Indian Ocean dipole mode. *SOLA,* **5,** 69–72, doi:10.2151/sola.2009-018.

Izumo, T., C. de Boyer Montegut, J.-J. Luo, S. K. Behera, S. Masson, and T. Yamagata, 2008: The role of the western Arabian Sea upwelling in Indian monsoon variability. *J. Climate,* **21,** 5603–5623, doi:10.1175/2008JCLI2158.1.

——, S. Masson, J. Vialard, C. de Boyer Montegut, S. K. Behera, G. Madec, K. Takahashi, and T. Yamagata, 2010: Low and high frequency Madden–Julian oscillations in austral summer: Interannual variations. *Climate Dyn.,* **35,** 669–683, doi:10.1007/s00382-009-0655-z.

Jayakumar, A., and C. Gnanaseelan, 2012: Anomalous intraseasonal events in the thermocline ridge region of southern tropical Indian Ocean and their regional impacts. *J. Geophys. Res.,* **117,** C03021, doi:10.1029/2011JC007357.

——, J. Vialard, M. Lengaigne, C. Gnanaseelan, J. P. McCreary, and B. Praveen Kumar, 2011: Processes controlling the surface temperature signature of the Madden–Julian oscillation in the thermocline ridge of the Indian Ocean. *Climate Dyn.,* **37,** 2217–2234, doi:10.1007/s00382-010-0953-5.

Jochum, M., and R. Murtugudde, 2005: Internal variability of Indian Ocean SST. *J. Climate,* **18,** 3726–3738, doi:10.1175/JCLI3488.1.

Kalnay, E., and Coauthors, 1996: The NCEP/NCAR 40-Year Reanalysis Project. *Bull. Amer. Meteor. Soc.,* **77,** 437–471, doi:10.1175/1520-0477(1996)077<0437:TNYRP>2.0.CO;2.

Kara, A. B., H. E. Hurlburt, and A. J. Wallcraft, 2005: Stability-dependent exchange coefficients for air–sea fluxes. *J. Atmos. Oceanic Technol.,* **22,** 1080–1094, doi:10.1175/JTECH1747.1.

——, A. J. Wallcraft, P. J. Martin, and E. P. Chassignet, 2008: Performance of mixed layer models in simulating SST in the equatorial Pacific Ocean. *J. Geophys. Res.,* **113,** C02020, doi:10.1029/2007JC004250.

Keerthi, M., M. Lengaigne, J. Vialard, C. de Boyer Montégut, and P. Muraleedharan, 2013: Interannual variability of the tropical Indian Ocean mixed layer depth. *Climate Dyn.,* **40,** 743–759, doi:10.1007/s00382-012-1295-2.

Knutson, T. R., and K. M. Weickmann, 1987: 30–60 day atmospheric oscillations: Composite life cycles of convection and circulation anomalies. *Mon. Wea. Rev.,* **115,** 1407–1436, doi:10.1175/1520-0493(1987)115<1407:DAOCLC>2.0.CO;2.

Kummerow, C., W. Barnes, T. Kozu, J. Shiue, and J. Simpson, 1998: The Tropical Rainfall Measuring Mission (TRMM) sensor package. *J. Atmos. Oceanic Technol.,* **15,** 809–817, doi:10.1175/1520-0426(1998)015<0809:TTRMMT>2.0.CO;2.

Lau, W. K., D. E. Waliser, K. Sperber, J. Slingo, and P. Inness, 2012: Modeling intraseasonal variability. *Intraseasonal Variability in the Atmosphere-Ocean Climate System,* Springer, 399–431.

Li, T., F. Tam, X. Fu, T. Zhou, and W. Zhu, 2008: Causes of the intraseasonal SST variability in the tropical Indian Ocean. *Atmos. Oceanic Sci. Lett.,* **1,** 18–23.

Li, Y., W. Han, T. Shinoda, C. Wang, R.-C. Lien, J. N. Moum, and J.-W. Wang, 2013: Effects of the diurnal cycle in solar radiation on the tropical Indian Ocean mixed layer variability during wintertime Madden–Julian oscillations. *J. Geophys. Res.,* **118,** 4945–4964, doi:10.1002/jgrc.20395.

Liebmann, B., and C. A. Smith, 1996: Description of a complete (interpolated), outgoing longwave radiation dataset. *Bull. Amer. Meteor. Soc.,* **77,** 1275–1277.

Lloyd, I. D., and G. A. Vecchi, 2010: Submonthly Indian Ocean cooling events and their interaction with large-scale conditions. *J. Climate,* **23,** 700–716, doi:10.1175/2009JCLI3067.1.

Locarnini, R. A., A. V. Mishonov, J. I. Antonov, T. P. Boyer, H. E. Garcia, O. K. Baranova, M. M. Zweng, and D. R. Johnson, 2010: *Temperature*. Vol. 1, *World Ocean Atlas 2009,* NOAA Atlas NESDIS 68, 184 pp.

Loeb, N. G., K. J. Priestley, D. P. Kratz, E. B. Geier, R. N. Green, B. A. Wielicki, P. O. R. Hinton, and S. K. Nolan, 2001: Determination of unfiltered radiances from the Clouds and the Earth's Radiant Energy System instrument. *J. Appl. Meteor.,* **40,** 822–835, doi:10.1175/1520-0450(2001)040<0822:DOURFT>2.0.CO;2.

Madden, R. A., and P. R. Julian, 1971: Detection of a 40–50 day oscillation in the zonal wind in the tropical Pacific. *J. Atmos. Sci.,* **28,** 702–708, doi:10.1175/1520-0469(1971)028<0702:DOADOI>2.0.CO;2.

Masumoto, Y., and G. Meyers, 1998: Forced Rossby waves in the southern tropical Indian Ocean. *J. Geophys. Res.,* **103,** 27 589–27 602, doi:10.1029/98JC02546.

McCreary, J. P., P. K. Kundu, and R. L. Molinari, 1993: A numerical investigation of dynamics, thermodynamics and mixed layer processes in the Indian Ocean. *Prog. Oceanogr.,* **31,** 181–244, doi:10.1016/0079-6611(93)90002-U.

McPhaden, M. J., and G. R. Foltz, 2013: Intraseasonal variations in the surface layer heat balance of the central equatorial Indian Ocean: The importance of zonal advection and vertical mixing. *Geophys. Res. Lett.,* **40,** 2737–2741, doi:10.1002/grl.50536.

——, and Coauthors, 2009: RAMA: The Research Moored Array for African–Asian–Australian Monsoon Analysis and Prediction. *Bull. Amer. Meteor. Soc.,* **90,** 459–480, doi:10.1175/2008BAMS2608.1.

Meehl, G. A., 1997: The South Asian monsoon and the tropospheric biennial oscillation. *J. Climate,* **10,** 1921–1943, doi:10.1175/1520-0442(1997)010<1921:TSAMAT>2.0.CO;2.

——, and J. M. Arblaster, 2002: The tropospheric biennial oscillation and Asian–Australian monsoon rainfall. *J. Climate,* **15,** 722–744, doi:10.1175/1520-0442(2002)015<0722:TTBOAA>2.0.CO;2.

——, ——, and J. Loschnigg, 2003: Coupled ocean–atmosphere dynamical processes in the tropical Indian and Pacific Oceans and the TBO. *J. Climate,* **16,** 2138–2158, doi:10.1175/2767.1.

Papa, F., F. Durand, W. B. Rossow, A. Rahman, and S. K. Bala, 2010: Satellite altimeter-derived monthly discharge of the Ganga–Brahmaputra River and its seasonal to interannual variations from 1993 to 2008. *J. Geophys. Res.,* **115,** C12013, doi:10.1029/2009JC006075.

Pohl, B., and A. J. Matthews, 2007: Observed changes in the lifetime and amplitude of the Madden–Julian oscillation associated with interannual ENSO sea surface temperature anomalies. *J. Climate,* **20,** 2659–2674, doi:10.1175/JCLI4230.1.

Rao, S. A., and S. K. Behera, 2005: Subsurface influence on SST in the tropical Indian Ocean: Structure and interannual variability. *Dyn. Atmos. Oceans,* **39,** 103–135, doi:10.1016/j.dynatmoce.2004.10.014.

Saji, N., B. Goswami, P. Vinayachandran, and T. Yamagata, 1999: A dipole mode in the tropical Indian Ocean. *Nature,* **401,** 360–363.

——, S. P. Xie, and C. Y. Tam, 2006: Satellite observations of intense intraseasonal cooling events in the tropical south Indian Ocean. *Geophys. Res. Lett.,* **33,** L14704, doi:10.1029/2006GL026525.

Sato, N., C. Takahashi, A. Seiki, K. Yoneyama, R. Shirooka, and Y. Takayabu, 2009: An evaluation of the reproducibility of the Madden–Julian oscillation in the CMIP3 multi-models. *J. Meteor. Soc. Japan,* **87,** 791–805, doi:10.2151/jmsj.87.791.

Schiller, A., and J. Godfrey, 2003: Indian Ocean intraseasonal variability in an ocean general circulation model. *J. Climate,* **16,** 21–39, doi:10.1175/1520-0442(2003)016<0021:IOIVIA>2.0.CO;2.

Sengupta, D., B. N. Goswami, and R. Senan, 2001: Coherent intraseasonal oscillations of ocean and atmosphere during the Asian summer monsoon. *Geophys. Res. Lett.,* **28,** 4127–4130, doi:10.1029/2001GL013587.

Shinoda, T., 2005: Impact of the diurnal cycle of solar radiation on intraseasonal SST variability in the western equatorial Pacific. *J. Climate,* **18,** 2628–2636, doi:10.1175/JCLI3432.1.

——, and H. H. Hendon, 1998: Mixed layer modeling of intraseasonal variability in the tropical western Pacific and Indian Oceans. *J. Climate,* **11,** 2668–2685, doi:10.1175/1520-0442(1998)011<2668:MLMOIV>2.0.CO;2.

——, and W. Han, 2005: Influence of the Indian Ocean dipole on atmospheric subseasonal variability. *J. Climate,* **18,** 3891–3909, doi:10.1175/JCLI3510.1.

——, P. E. Roundy, and G. N. Kiladis, 2008: Variability of intraseasonal Kelvin waves in the equatorial Pacific Ocean. *J. Phys. Oceanogr.,* **38,** 921–944, doi:10.1175/2007JPO3815.1.

——, W. Han, E. J. Metzger, and H. E. Hurlburt, 2012: Seasonal variation of the Indonesian Throughflow in Makassar Strait. *J. Phys. Oceanogr.,* **42,** 1099–1123, doi:10.1175/JPO-D-11-0120.1.

——, T. Jensen, M. Flatau, W. Han, and C. Wang, 2013: Large-scale oceanic variability associated with the Madden–Julian oscillation during the CINDY/DYNAMO field campaign from satellite observations. *Remote Sens.,* **5,** 2072–2092, doi:10.3390/rs5052072.

Sperber, K. R., S. Gualdi, S. Legutke, and V. Gayler, 2005: The Madden–Julian oscillation in ECHAM4 coupled and uncoupled general circulation models. *Climate Dyn.,* **25,** 117–140, doi:10.1007/s00382-005-0026-3.

Tozuka, T., T. Yokoi, and T. Yamagata, 2010: A modeling study of interannual variations of the Seychelles Dome. *J. Geophys. Res.,* **115,** C04005, doi:10.1029/2009JC005547.

Vialard, J., G. Foltz, M. J. McPhaden, J. P. Duvel, and C. de Boyer Montégut, 2008: Strong Indian Ocean sea surface temperature signals associated with the Madden–Julian oscillation in late 2007 and early 2008. *Geophys. Res. Lett.,* **35,** L19608, doi:10.1029/2008GL035238.

——, and Coauthors, 2009: Cirene: Air–sea interactions in the Seychelles–Chagos thermocline ridge region. *Bull. Amer. Meteor. Soc.,* **90,** 45–61, doi:10.1175/2008BAMS2499.1.

——, A. Jayakumar, C. Gnanaseelan, M. Lengaigne, D. Sengupta, and B. Goswami, 2012: Processes of 30–90 days sea surface temperature variability in the northern Indian Ocean during boreal summer. *Climate Dyn.,* **38,** 1901–1916, doi:10.1007/s00382-011-1015-3.

Vinayachandran, P., and N. Saji, 2008: Mechanisms of south Indian Ocean intraseasonal cooling. *Geophys. Res. Lett.,* **35,** L23607, doi:10.1029/2008GL035733.

Waliser, D. E., 2005: Intraseasonal variability. *The Asian Monsoon,* B. Wang, Ed., Springer, 844 pp.

——, K. Lau, and J. H. Kim, 1999: The influence of coupled sea surface temperatures on the Madden–Julian oscillation: A model perturbation experiment. *J. Atmos. Sci.,* **56,** 333–358, doi:10.1175/1520-0469(1999)056<0333:TIOCSS>2.0.CO;2.

Wallcraft, A. J., E. J. Metzger, and S. N. Carroll, 2009: Software design description for the Hybrid Coordinate Ocean Model (HYCOM) version 2.2. Naval Research Laboratory Stennis Space Center Tech. Rep. NRL/MR/7320-09-9166, 149 pp.

Wang, B., and H. Rui, 1990: Synoptic climatology of transient tropical intraseasonal convection anomalies: 1975–1985. *Meteor. Atmos. Phys.,* **44,** 43–61, doi:10.1007/BF01026810.

——, and X. S. Xie, 1998: Coupled modes of the warm pool climate system. Part 1: The role of air–sea interaction in maintaining Madden–Julian oscillation. *J. Climate,* **11,** 2116–2135, doi:10.1175/1520-0442-11.8.2116.

Wang, J.-W., W. Han, and R. L. Sriver, 2012a: Impact of tropical cyclones on the ocean heat budget in the Bay of Bengal during 1999: 1. Model configuration and evaluation. *J. Geophys. Res.,* **117,** C09020, doi:10.1029/2012JC008372.

——, ——, and ——, 2012b: Impact of tropical cyclones on the ocean heat budget in the Bay of Bengal during 1999: 2. Processes and interpretations. *J. Geophys. Res.,* **117,** C09021, doi:10.1029/2012JC008373.

Watterson, I., and J. Syktus, 2007: The influence of air–sea interaction on the Madden–Julian oscillation: The role of the seasonal mean state. *Climate Dyn.,* **28,** 703–722, doi:10.1007/s00382-006-0206-9.

Webber, B. G., A. J. Matthews, and K. J. Heywood, 2010: A dynamical ocean feedback mechanism for the Madden–Julian oscillation. *Quart. J. Roy. Meteor. Soc.,* **136,** 740–754, doi:10.1002/qj.604.

——, ——, ——, and D. P. Stevens, 2012a: Ocean Rossby waves as a triggering mechanism for primary Madden–Julian events. *Quart. J. Roy. Meteor. Soc.,* **138,** 514–527, doi:10.1002/qj.936.

——, D. P. Stevens, A. J. Matthews, and K. J. Heywood, 2012b: Dynamical ocean forcing of the Madden–Julian oscillation at lead times of up to five months. *J. Climate,* **25,** 2824–2842, doi:10.1175/JCLI-D-11-00268.1.

Wentz, F. J., C. Gentemann, D. Smith, and D. Chelton, 2000: Satellite measurements of sea surface temperature through clouds. *Science,* **288,** 847–850, doi:10.1126/science.288.5467.847.

Wheeler, M. C., and H. H. Hendon, 2004: An all-season real-time multivariate MJO index: Development of an index for monitoring and prediction. *Mon. Wea. Rev.,* **132,** 1917–1932, doi:10.1175/1520-0493(2004)132<1917:AARMMI>2.0.CO;2.

Wielicki, B. A., B. R. Barkstrom, E. F. Harrison, R. B. Lee III, G. Louis Smith, and J. E. Cooper, 1996: Clouds and the Earth's Radiant Energy System (CERES): An Earth observing system experiment. *Bull. Amer. Meteor. Soc.,* **77,** 853–868, doi:10.1175/1520-0477(1996)077<0853:CATERE>2.0.CO;2.

Woolnough, S. J., J. M. Slingo, and B. J. Hoskins, 2000: The relationship between convection and sea surface temperature on intraseasonal timescales. *J. Climate,* **13,** 2086–2104, doi:10.1175/1520-0442(2000)013<2086:TRBCAS>2.0.CO;2.

——, ——, and ——, 2001: The organization of tropical convection by intraseasonal sea surface temperature anomalies. *Quart. J. Roy. Meteor. Soc.,* **127,** 887–907, doi:10.1002/qj.49712757310.

——, F. Vitart, and M. Balmaseda, 2007: The role of the ocean in the Madden–Julian oscillation: Implications for MJO prediction. *Quart. J. Roy. Meteor. Soc.,* **133,** 117–128, doi:10.1002/qj.4.

Xavier, P. K., 2012: Intraseasonal convective moistening in CMIP3 models. *J. Climate,* **25,** 2569–2577, doi:10.1175/JCLI-D-11-00427.1.

Xie, S.-P., H. Annamalai, F. A. Schott, and J. P. McCreary, 2002: Structure and mechanisms of south Indian Ocean climate variability. *J. Climate,* **15,** 864–878, doi:10.1175/1520-0442(2002)015<0864:SAMOSI>2.0.CO;2.

Yokoi, T., T. Tozuka, and T. Yamagata, 2008: Seasonal variation of the Seychelles Dome. *J. Climate,* **21,** 3740–3754, doi:10.1175/2008JCLI1957.1.

——, ——, and ——, 2009: Seasonal variations of the Seychelles Dome simulated in the CMIP3 models. *J. Phys. Oceanogr.,* **39,** 449–457, doi:10.1175/2008JPO3914.1.

——, ——, and ——, 2012: Seasonal and interannual variations of the SST above the Seychelles Dome. *J. Climate,* **25,** 800–814, doi:10.1175/JCLI-D-10-05001.1.

Zhang, C., 2005: Madden–Julian oscillation. *Rev. Geophys.,* **43,** RG2003, doi:10.1029/2004RG000158.

——, M. Dong, S. Gualdi, H. H. Hendon, E. D. Maloney, A. Marshall, K. R. Sperber, and W. Wang, 2006: Simulations of the Madden–Julian oscillation in four pairs of coupled and uncoupled models. *Climate Dyn.,* **27,** 573–592, doi:10.1007/s00382-006-0148-2.

——, J. Gottschalck, E. D. Maloney, M. W. Moncrieff, F. Vitart, D. E. Waliser, B. Wang, and M. C. Wheeler, 2013: Cracking the MJO nut. *Geophys. Res. Lett.,* **40,** 1223–1230, doi:10.1002/grl.50244.

Zhang, X., Y. Lu, K. R. Thompson, J. Jiang, and H. Ritchie, 2010: Tropical Pacific Ocean and the Madden–Julian Oscillation: Role of wind and buoyancy forcing. *J. Geophys. Res.,* **115,** C05022, doi:10.1029/2009JC005734.

Zhao, C., T. Li, and T. Zhou, 2013: Precursor signals and processes associated with MJO initiation over the tropical Indian Ocean. *J. Climate,* **26,** 291–307, doi:10.1175/JCLI-D-12-00113.1.

Zhou, L., R. Murtugudde, and M. Jochum, 2008: Dynamics of the intraseasonal oscillations in the Indian Ocean South Equatorial Current. *J. Phys. Oceanogr.,* **38,** 121–132, doi:10.1175/2007JPO3730.1.